

# Using a data-driven statistical model to better evaluate surface turbulent heat fluxes in weather and climate numerical models: a demonstration study

Maurin ZOUZOUA <sup>1</sup>, Sophie BASTIN <sup>1</sup>, Fabienne LOHOU <sup>2</sup>, Marie LOTHON <sup>2</sup>, Marjolaine CHIRIACO <sup>1</sup>, Mathilde JOME <sup>2</sup>, Cécile MALLET <sup>1</sup>, Laurent BARTHES <sup>1</sup>, Guylaine CANUT <sup>3</sup>, and <sup>2</sup>

<sup>1</sup>LATMOS/IPSL, UVSQ Université Paris-saclay, Sorbonne Université, CNRS, CNES, Guyancourt, France

<sup>2</sup>Centre de Recherches Atmosphériques (CRA)/Laboratoire d'Aérodynamique de Toulouse (LAERO), France

<sup>3</sup>Centre National de Recherches Météorologiques (CNRM)/Météo-France

**Correspondence:** (maurin.zouzoua@latmos.ipsl.fr)

**Abstract.** This study proposes ~~the use of~~ using a data-driven statistical model to freeze ~~the~~ errors due to differences in environmental forcing when evaluating ~~the~~ surface turbulent heat fluxes from weather and climate numerical models with ~~the~~ observations. It takes advantage of continuous acquisition over approximately ten years of near-surface sensible and latent heat fluxes ( $H$  and  $LE$  respectively) together with ancillary parameters over the supersite "“Météopole”" of the French national research infrastructure ACTRIS-FR, located in Toulouse. The statistical model consists of several multi-layer perceptrons (MLPs) with the same architecture. Thirteen variables characterizing ~~the~~ environmental forcing in the surface layer ~~at an hourly time scale~~ on an hourly timescale are used as input parameters to ~~estimate simultaneously~~ estimate the observed  $H$  and  $LE$  ~~simultaneously~~. The MLPs are trained using 5-year observational data under a 5-fold cross-validation. The remaining data ~~is~~ are used to test the estimates ~~on~~ under unknown conditions. ~~A case study is performed with data from a regional climate simulation.~~ The performance of the statistical model ranges within the state-of-the-art surface ~~parametrization~~ parameterization schemes on hourly and seasonal time scales. It ~~has also~~ also has a good generalization ability, but ~~it~~ hardly estimates negative  $H$  and large  $LE$ . ~~A case study is conducted with data from a regional climate simulation.~~ The statistical model is used to evaluate the simulated fluxes ~~under in~~ the simulated environment to better examine the flaws of their numerical formulation throughout the simulation. Comparison of simulated fluxes with observed and MLP-based fluxes ~~show~~ shows different results. According to MLP-based

15 fluxes in the simulated environment, the land surface scheme of this climate model tends to underestimate large sensible heat flux. Thus, it incorrectly partitions between surface heating and evaporation during the late summer. Our innovative method provides insight into ~~differently evaluating the~~ different techniques for evaluating simulated near-surface turbulent heat fluxes when a long period of comprehensive observations is available. It can usefully support ongoing efforts ~~for improvements of~~ surface parametrization to improve surface parameterization schemes.

The surface sensible heat ( $H$ ) and latent heat ( $LE$ ) fluxes describe the surface-atmosphere exchanges of heat and moisture (Stull, 1988). They are major terms of the Surface-Energy-Budget (SEB) and key drivers of the atmospheric boundary layer (ABL) ~~processes~~ processes, such as turbulent mixing and convective cloud formation. Numerical models are important tools for weather forecasting and climate projection. Due to the coarse spatio-temporal resolution of operational weather and climate numerical models, the surface turbulent heat fluxes are computed with the help of surface parametrization schemes, which have different levels of sophistication. The correct ~~representation~~ formulation of turbulent heat fluxes by these schemes is then necessary for properly simulating the surface-atmosphere interactions. However, ~~this representation is the second most important source of biases in simulations with the numerical models (Zadra et al., 2018). It is therefore the representation of convection and surface processes are the two most important sources of systematic biases in numerical simulations~~ (Zadra et al., 2018; Frassoni et al., 2023). Therefore, it is of paramount importance to develop improvements, and evaluation is crucial to provide guidance.

The ~~strategies for evaluating surface parametrization schemes can be roughly classified into two main approaches (Henderson-Sellers et al., 1996). The first involves running full numerical simulations, with meteorological forcing and surface turbulent heat fluxes interacting mutually. The simulated surface turbulent heat fluxes are then confronted with observations. This approach blends many sources of errors such as inconsistent landscape representation (vegetation and soil characteristics) and inaccurate~~ evaluation of surface turbulent fluxes is a real issue due to the number of factors that can explain the differences. These factors include inaccuracies in simulated weather conditions (such as cloudiness, temperature, ~~moisture~~, wind, etc.). It is likely a useful method for assessing how well a numerical model is working. However, the formulations that ~~resolve the surface-atmosphere interactions cannot be unambiguously evaluated since the simulated turbulent fluxes are related to simulated weather conditions that are not necessarily observed~~ wind, moisture, and surface stability), inconsistencies in landscape representation within the numerical model (e.g., vegetation and soil characteristics), the lack of representativeness of local measurements compared to the model grid scale, uncertainties in observations (Mauder et al., 2020), and finally, the parameterization of fluxes, which typically relies on Monin-Obukhov similarity theory (MOST, Monin and Obukhov, 1954).

Various strategies using ~~full numerical simulation~~ coupled numerical simulations have been proposed to reduce ~~the sources of errors, for example by~~ biases related to weather conditions, the scope of our proposed method here. These include investigating the relationships between surface heat fluxes and ~~driving atmospheric variables~~ atmospheric variables pairwise (e.g., Zhou and Wang, 2016; Bastin et al., 2018). ~~Nevertheless, there are still large uncertainties. The second approach suppresses the~~

errors associated with the simulated weather conditions by externalizing the surface scheme to the numerical model. The  
50 ~~turbulent fluxes are then computed thanks to~~ or focusing on clear-sky conditions (e.g., Arjdal et al., 2024). Another approach  
involves using the land surface model in offline mode (e.g., Liu et al., 2013), where turbulent heat fluxes are computed using  
input from observations or reanalysis. ~~However, the crucial influence of turbulence fluxes on weather conditions is not taken~~  
~~into account. Moreover, the representativity of surface characteristics remains problematic because several required properties~~  
~~(roughness length, soil and vegetation parameters, etc.) are not usually observed. The use of their default or empirical values is~~  
55 ~~an additional source of uncertainties (Liu et al., 2013).~~ The intrinsic limitations of these two approaches demonstrate the need  
~~for another to reliably evaluate the numerical formulation of turbulent heat fluxes.~~ While these methods are encouraging, they  
have limitations that prevent drawing general conclusions.

In recent years, machine learning techniques have known a tremendous expansion in weather and climate sciences (de  
60 Burgh-Day and Leeuwenburg, 2023), driven by unrivalled results and infinite possibilities. ~~Due to~~ Because of their ability to  
act as universal approximators ~~-(Cybenko, 1989; Hornik et al., 1989), Artificial Neural Networks (ANNs) have emerged as~~  
a powerful tool in machine learning ~~-(Goodfellow et al., 2016)~~ for data-driven statistical modelling (Goodfellow et al., 2016)  
. They can effectively model a broad range of complex relationships for quantitative ~~modellings~~ approximations, such as  
multivariate classification and regression ~~-(Zhang, 2008; Kruse et al., 2013).~~ ANNs are generally used to overcome the  
65 limitations of classical approaches. Several studies have explored the use of ANN-based estimators for replacing numerical  
atmospheric models or some of their components (e.g., Bonavita and Laloyaux, 2020; Gentine et al., 2018; Knutti et al.,  
2003; Sarghini et al., 2003; Vollant et al., 2017). In the study of Abramowitz (2005), a trained ANN with observational data is  
used as a benchmark to objectively assess how well a land surface scheme should perform in estimating turbulent heat and net  
CO<sub>2</sub> fluxes. Recently, Leufen and Schädler (2019) estimated the scaling quantities needed in some surface parameterization  
70 schemes to calculate the momentum and sensible heat fluxes using an ANN-based model driven by meteorological factors.  
The ANN has learned from multi-year comprehensive data collected over several types of landscapes (grassland, forest, etc.).  
They obtained satisfying results when this ANN was implemented to replace the similarity functions in a one-dimensional  
stand-alone land surface model. In the field of hydrology, ANN-based models are increasingly being employed to estimate  
reliable evapotranspiration for near real-time monitoring of crop water demand (Kumar et al., 2011; Kelley et al., 2020; Kelley  
75 and Pardyjak, 2019). The growing availability of comprehensive data from atmospheric observatories offers an opportunity  
to explore ANN-based methods to better evaluate the numerical formulation of surface  $H$  and  $LE$ , particularly within the

framework of full simulations, which is the ultimate goal of numerical models.

The Model and Observation for Surface-Atmosphere Interactions (MOSAI) project (Lohou et al., 2022) ~~aims to contribute to a better~~ seeks to enhance the understanding of surface-atmosphere interactions ~~to improve their representation in weather and climate numerical models. One of the principal objectives is to propose.~~ The key objectives are to address the issue of observations representativity and uncertainty, encourage the development of novel methods to better compare simulations with observations, and improve surface heat fluxes parametrization over heterogeneous surfaces. This paper is a contribution to the second objective. It proposes a novel method to diagnose the errors of numerical models in their formulations of  $H$  and  $LE$ . The idea is to exploit the capabilities of machine learning techniques on multi-years of continuous observational data, rather than performing a classical direct comparison of simulated against observed fluxes. ~~This paper is a contribution to this objective.~~ It presents a pilot study that uses data collected during several years at a ~~French flux~~ permanent French station, operational since June 2012, for evaluating turbulent heat fluxes in a climate numerical model over the period from 01 January 2012 to 31 December 2016. Section 2 presents the proposed evaluation approach, which involves using observational data to build a data-driven statistical model that ~~estimates~~ approximates observed  $H$  and  $LE$ . The data and methods of our experimental setup are described in section 3. Section 4 discusses the performance of the data-driven model in observed conditions. In ~~the~~ section 5, the data-driven model is applied to simulated conditions to better identify the flaws in the numerical formulation of turbulent heat fluxes. Finally, section 6 delivers a conclusion.

## 2 Justification and objectives

The ~~fluxes  $H$  and  $LE$~~  surface turbulent heat fluxes are primarily governed by the net radiative flux ( $R_{net}$ ) ~~at the surface,~~ which is the algebraic sum of incoming ( $\downarrow$ ) and outgoing ( $\uparrow$ ) ~~longwave (LW) and shortwave (SW)~~ long-wave (LW) and short-wave (SW) radiations. Their magnitude is ~~as well determined by thermodynamical~~ strongly linked to thermodynamic and dynamical conditions ~~within in~~ the surface layer; a thin atmospheric layer immediately above the ground ~~in which the~~ where turbulent fluxes are approximately constant. The flux  $H$  is responsible for removing/depositing heat from/to the ground, and  $LE$  is the energy exchanged through phase changes of water from liquid (or ice) to vapour.  $H$  and  $LE$  are therefore closely linked to the vertical gradients of temperature and humidity in the surface layer. The relative predominance between  $H$  and  $LE$  depends on surface characteristics (vegetation and soil moisture),  $LE$  is predominant over wet surfaces and ~~vice-versa. Solar heating and the intra-annual~~ vice versa. The solar heating and annual evolution of land cover induce diurnal and seasonal cycles of

105 turbulent heat fluxes. Thus, the turbulent fluxes result from complex non-linear relationships between meteorological factors, surface cover and soil conditions.

~~Current~~ The vast majority of numerical formulations of turbulent heat fluxes ~~are largely based upon~~ rely on the validity of ~~the Monin-Obukhov similarity theory (MOST, Monin and Obukhov, 1954)~~ MOST in the surface layer, which ~~relies on~~ assumes horizontally homogeneous terrain, and fair and steady-state ~~meteorological-atmospheric~~ conditions. The fluxes are then expressed in terms of the vertical gradient of the corresponding ~~quantity (temperature and humidity thermodynamic scalar (temperature for  $H$  and humidity for  $LE$  resp.) within this layer and,)~~ in the surface layer, along with various parameters describing ~~soil-ground~~ wetness and roughness. The weather and climate models usually apply MOST between the ground and the ~~lowest-atmospheric-level~~ first atmospheric level above, considered as the top of the surface layer (Liu et al., 2013).  
115 However, the relevance of this theory in grid cells with heterogeneous land use is highly questionable.

Another fundamental relationship, ~~that is~~ usually used in ~~these~~ numerical models, is the conservation of SEB as follows:

$$R_{net} = H + LE + G \quad (1)$$

~~Where~~ where  $G$  is the ground heat flux. However, this conservation is rarely verified when  $H$  and  $LE$  are measured with an  
120 Eddy-Covariance (EC) method, the most recent and reliable technique (Mauder and Foken, 2004; Wolf et al., 2008; Aubinet et al., 2012). Indeed, the available energy  $R_{net} - G$  is very often greater than the total turbulent flux  $H + LE$ , especially over a heterogeneous surface (Hu et al., 2021; Mauder et al., 2018; Foken et al., 2011). This imbalance can be quantified by the residual energy (~~RES~~ RES).

$$125 \quad RES(\%) = 100 \cdot \frac{(R_{net} - G) - (H + LE)}{R_{net} - G} \quad (2)$$

Thus, the ~~discrepancy between~~ discrepancies in simulated and observed  ~~$H$  and  $LE$  may arise, on the one hand, to incorrect parametrizations and, on the other hand, due to both observation and model biases. The~~ surface turbulent heat fluxes could stem from inconsistencies in surface representativeness, process parametrization, or observational and modeling biases. Therefore, a  
130 direct comparison is ~~therefore less useful to point out the errors inherent to numerical~~ less useful in identifying the weaknesses

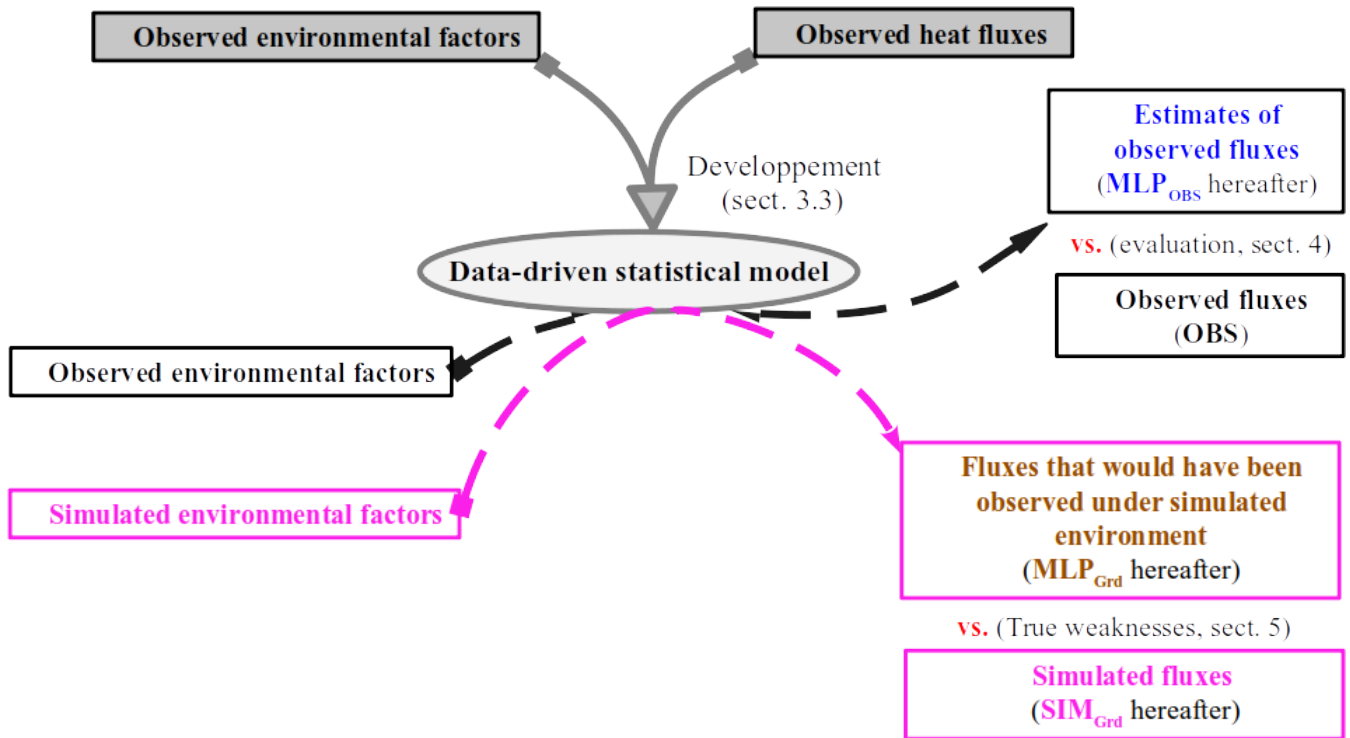


**Figure 1.** Schematic illustration of our proposed evaluation method. [See the text for more details](#)

of the surface parameterization scheme for the formulations of  $H$  and  $LE$ . The study by Abramowitz (2005), based on observational data, is a pioneer in using a data-driven statistical model to reliably assess land surface schemes. Inspired by the methodology of this study, we propose an evaluation approach ~~dedicated to a~~ specifically devoted to full numerical simulation that ~~includes a more realistic representation of~~ realistically represents the interplay between surface turbulent heat fluxes and environmental factors. ~~It~~ This approach consists of two successive phases that are illustrated in Figure 1. At first, a long period of  ~~$H$  and  $LE$  observations together with related~~ observations of turbulent heat fluxes and relevant environmental factors is ~~required~~ needed to build a data-driven statistical model ~~estimating  $H$  and  $LE$~~  that approximates observed heat fluxes. It can be regarded as a ~~parameterization~~ parameterization without any simplifying assumptions. Then, the application of this statistical model to the simulated environment ~~will generate~~ generates the fluxes that would have been observed under this environment from a statistical point of view. Thus, by comparing simulated heat fluxes with their corresponding statistically-based ~~estimates~~ estimates ~~corresponding to the simulated fluxes for the same~~ environment, the ~~uncertainties due to model biases~~ biases from other components of the numerical model are frozen. This allows us to better ~~diagnose~~ isolate the weaknesses in the formulations of  $H$  and  $LE$  ~~formulations~~ formulations, or due to the surface parameters and characteristics. The problems of observation representativeness

and uncertainty are not addressed here. However, *RES* will be used as an indicator of the reliability of the observation in our analysis. The use of an indicator of the representativeness of observation is also in development but is out of the scope of this paper.

### 3 Experimental setup

#### 3.1 Observational data

This pilot study is based on high-temporal-resolution data gathered over several years at the Météopole (43.57°N, 1.374°E, 157 m above sea level, Etienne, 2022), a measurement site hosted by the Centre National de Recherches Météorologiques (CNRM) in Toulouse, France. This site, operated by ~~Meteo-France~~ Météo-France, is part of the Aerosol, Clouds and Trace Gases Research Infrastructure (~~ACTRIS~~ in France (ACTRIS-FR)). The observation facility consists of several co-located ground-based instruments installed in a large grass field. ~~The AERIS platform () provides free access to this dataset.~~

~~Since 15 June~~ Starting from 24 November 2012, the surface energy budget and the corresponding environmental forcing (soil and overlying meteorological conditions) are continuously documented through a comprehensive set of ~~parameters documenting soil conditions, overlying meteorological forcing and surface energy budget is collected. The most relevant ones measurements; the most relevant~~ for our study are listed in Table 1. ~~These include soil heat flux~~ In addition to turbulent fluxes  $H$  and  $LE$ , these include the four components of the radiative budget, ground heat flux  $G$ , the four radiative flux components, ~~dry~~ air temperature ( $T$ ) and relative humidity ( $RH$ ) at ~~the~~ two conventional heights 2 and 10 m above ground level (agl), surface pressure ( $SP$ ) and rainfall ( $RR$ ), and soil volumetric water content ( $SWC$ ). ~~They are originally acquired every 1 min and finally archived as half-hourly averages. These data undergo several quality checks before being released to the public.~~ The surface and soil temperature are also measured at the Météopole station, but there is a lack of data before 12 July 2015. We then ~~opted~~ decided not to use these measurements to avoid limiting the number of samples, which is crucial when building a data-driven statistical model. Sensitivity analysis indicates no significant loss of key information concerning the variability in  $H$  and  $LE$ .

The ~~near-surface sensible (fluxes  $H$ ) and latent (and  $LE$ ) heat fluxes are estimated~~ are measured with the EC method (Aubinet et al., 2012) ~~based on by~~ high-frequency measurements (20 Hz) of ~~the wind 3D components~~ three-dimensional components of the wind,  $T$  and water vapour specific humidity ( $q$ ) ~~at 3.7, with~~ with a sonic anemometer

and ~~rapid-hygrometer respectively. a rapid hygrometer mounted at 3.7 magl. Eventually,~~ EddyPro 7 software (<https://www.licor.com/env/support/EddyPro/software.html>) is ~~used to compute the fluxes over half-hourly samples.~~ ~~Quality flags, defined according to Mauder and Foken (2004), rank the measurements into three different~~ utilized to compute turbulent heat fluxes at a half-hour temporal resolution. Each of these observed fluxes is accompanied by a quality flag by

175 Mauder and Foken (2004) that ranks the measurement into three categories: 0 for ~~the best high~~ quality, 1 for ~~the suitable~~ suitable to be used for research and 2 for ~~those~~ that should not be used ~~for analysis~~. Besides, the ~~measurements of the used rapid-hygrometer~~ rapid hygrometer's accuracy (licor 7500 open-path) ~~are is~~ highly degraded in wet conditions (fog ~~and rain~~ ). ~~Thus or rain event~~. Therefore, the turbulent fluxes are normally not estimated ~~in under~~ these conditions, based on the sensor ~~diagnostic and the detection of~~ rainfall occurrence. However, wrong measurements could still be performed, as an

180 accumulation of liquid water persists on the sensor.

The environmental parameters are originally acquired every 1-min and finally archived as half-hourly averages, matching the temporal resolution of turbulent fluxes. Jomé et al. (2023) analyzed the contribution of the surrounding land cover types to the turbulent heat fluxes measured at the ~~Météopole flux~~ Météopole station. It was found that the contribution of grass cover

185 ranges between 80 to 90 %, with the remaining contribution coming mostly from urbanized areas. The observational data from the Météopole station are freely available via the AERIS platform (<https://www.aeris-data.fr/>). This database undergoes several quality controls and is regularly updated after an annual exercise.

**Table 1.** Observational data from the Météopole ~~flux~~ station used in this study. A negative height corresponds to a soil depth.

Variables	height of acquisition (m a.g.l)
Surface upward/downward long/short-wave components	10
Turbulent heat fluxes ( $H$ and $LE$ ) and horizontal wind components ( $u$ , $v$ )	3.7
<del>Relative humidity (<math>RH</math>) and dry air temperature (<math>T</math>)</del> <u>Air temperature (<math>T</math>) and relative humidity (<math>RH</math>)</u>	2 and 10
surface pressure ( $SP$ ) and rainfall ( $RR$ )	-
<del>Heat flux into the ground</del> <u>Ground heat flux</u> ( $G$ )	-0.05
Soil volumetric water content ( $SWC$ )	at 16 levels, the first at -0.1

~~The data availability for the turbulent heat fluxes and ancillary parameters overlap continuously from 00:00 UTC 24~~

190 ~~November 2012. At the time of this study, This study is based on~~ the data collected ~~up to until~~ 23:30 UTC ~ UTC 31 December 2022 ~~have been released, which represents nearly 10 consecutive years of monitoring.~~ The corresponding database contains ~~117778 half-hourly time steps for which turbulent heat fluxes, meteorological and soil parameters~~ 117782 half-hours for which the required measurements (Table 1) are simultaneously available, i.e. nearly, almost 66.5 % of the samples



expected since 00 : 00 UTC 24 November 2012. ~~This percentage is highly affected by the lack of turbulent fluxes during~~ The  
195 lack of data is mainly due to the absence of observed turbulent fluxes, mostly under wet conditions. Since the quality and  
amount of the data on which the data-driven statistical model is built determines its performance, several considerations were  
applied to select the samples with the most reliable measurements ~~of  $H$  and  $LE$~~ . Firstly, only  $H$  and  $LE$  with the quality  
flag 0 or 1 (Mauder and Foken, 2004) were selected. Due to the strong evolution of ~~the surface heat fluxes along~~ continental  
turbulent heat fluxes throughout the day, several authors preferred to evaluate ~~the~~ numerical simulations under well-established  
200 diurnal cycles (e.g. Román-Cascón et al., 2021). ~~Then, secondly, we considered sampling at~~ For the final selection, we then  
considered sampling on a daily scale ~~when selecting the final observational data~~. The half-hourly data included in our analyses  
are collected during the diurnal cycles (starting at 00 : 00) that fulfil the ~~three following~~ following three conditions: (i) it is  
described by at least half of the expected samples (i.e., 24/48 of pre-selected samples), ~~(iii)~~ (ii) the daily cumulative rainfall is  
less than 5 mm and (iii) all the items of Pearson’s correlation coefficient matrix between  $H$ ,  $LE$  and  $SW^\downarrow$  are greater than 0.6.  
205 The two last criteria are a compromise to preserve a reasonable number of samples while reducing the amount of data possibly  
impacted by wet conditions. This leaves us with ~~66273–80683~~ half-hourly samples (~~about 56~~ around 69 % of all available  
samples), documenting ~~1983–2274~~ diurnal cycles. Figure 2a shows the distribution of these samples per year, and Figure 2b  
presents the distribution of the corresponding diurnal cycles per month. None of these diurnal cycles was fully sampled, the  
rate of data availability is around ~~70~~ 74 % on average. The annual cycles from 2015 to 2021 are relatively well sampled. The  
210 selected diurnal cycles are ~~overall homogeneously distributed over the year. The four homogeneously distributed throughout~~  
each year, meaning that the four typical seasons (winter, spring, summer, and autumn) are ~~therefore rather well covered. The~~  
~~annual cycles from 2015 to 2021 are particularly well sampled~~ represented well. There are no selected samples from June to  
September 2022 (Figure 2b) due to missing data of  $LW^\uparrow$ .

215

### 3.2 Numerical model data

To test our proposed evaluation method, we used data from an existing climate simulation, carried out with the Regional Earth  
system model of the Institut Pierre Simon Laplace (RegIPSL). Within the settings of this model, the land surface model OR-  
CHIDEE (ORganising Carbon and Hydrology In Dynamic EcosystEms, Krinner et al., 2005) provides the bottom boundary  
220 conditions for the continental surface to the atmospheric model WRF, WRF v3.7.1 (Weather Research and Forecasting, Ska-  
marock et al., 2008) ~~over the continental surface~~. The simulation has been ~~performed in~~ carried out within the framework of the

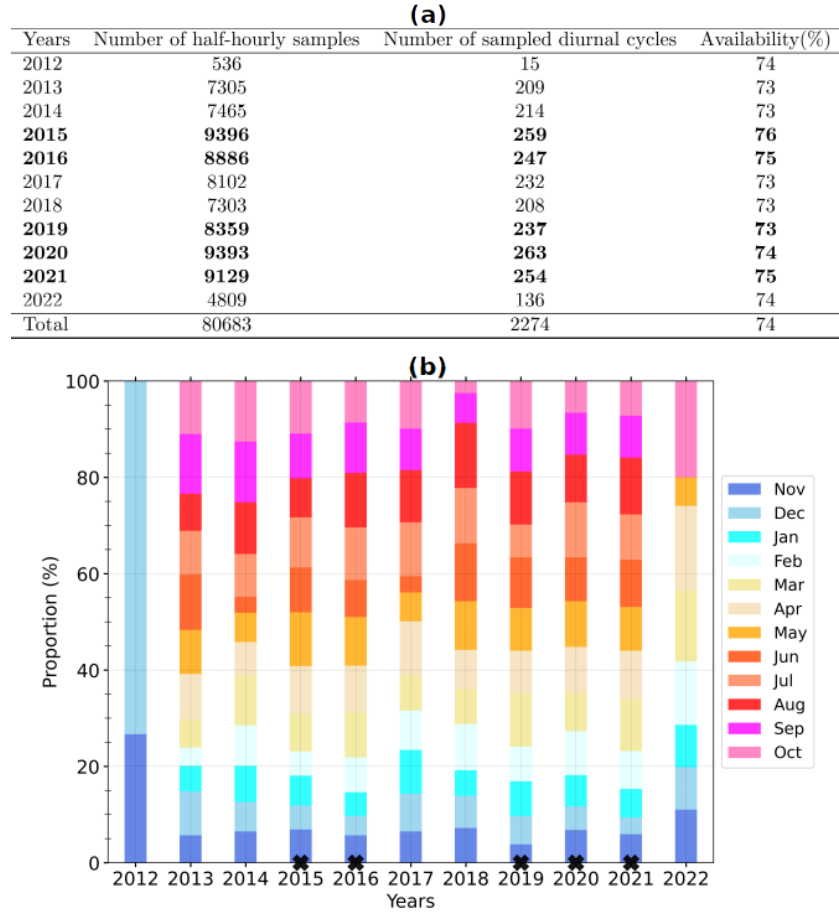


**Figure 2.** (a) Number of remaining half-hourly samples and diurnal cycles per year after the selection over the period from 24 November 2012 at 00 : 00 to 31 December 2022 at 23 : 30 (see text for details), and (b) monthly distribution of these diurnal cycles. The rate of availability is the ratio of the selected half-hourly samples (second column) over the number of samples which fully describe the corresponding diurnal cycles (48 times the third column). The data of the five most covered years (in bold (a), with a black cross at the bottom (b)) composed the learning set, the other years are used as the test set.

Mediterranean Coordinated Regional Climate Downscaling Experiment (Med-CORDEX) initiative (Ruti et al., 2016) and the European Climate Prediction ~~system~~ System (EUCP) H2020 project (Coppola et al., 2020). It covers the Euro-Mediterranean area with a horizontal resolution of 20 km on a Lambert-conformal projection and spans from 1<sup>st</sup> January 1979 to 31 December 2016. The atmospheric vertical column was discretized by 46 hybrid sigma-pressure levels (full ~~eta-levels~~ eta levels), with 16 levels roughly in the first 2 kmagl. The soil column, which extends ~~until to~~ to 2 m below the ground, was subdivided by 11 nodes. ~~Seven of these nodes were located in the top~~, with seven nodes located within the first 15 cm. For more details, ~~readers may the reader can~~ refer to the studies of Guion et al. (2022) which used this climate simulation to assess the impact of droughts and ~~heatwaves upon~~ heat waves on vegetation and wildfires in the ~~Western~~ western Mediterranean, and of Shahi et al.

230 (2022) which used the RegIPSL model to ~~analyse the added value~~ analyze the added value of a convective-permitting climate simulation over the Iberian ~~peninsula~~ Peninsula.

The landscape in ORCHIDEE was categorized into 13 main classes including bare soil and 12 Plant Functional Types (PFTs: eight for forests, two for grasslands and two for croplands). The total proportion of the grid cell occupied by each class remained constant throughout the simulation. Nonetheless, for PFTs, the proportion effectively occupied by vegetation was  
235 allowed to vary and the non-occupied fraction was defined as bare soil (Ducharne et al., 2018; Alléon, 2022). The bare soil fraction is assumed to contain the urbanized areas. For simulating the surface processes, ORCHIDEE requires several environmental parameters including surface precipitation, ~~downwelling~~ downward  $SW$  and  $LW$  as well as air temperature, humidity, and wind just above the ground. These were taken at the lowest vertical level of WRF, ~~which was~~ located within 20 magl. The near-surface turbulent heat fluxes are computed using bulk aerodynamic formulations (Ducoudré et al.,  
240 1993; Krinner et al., 2005; Alléon, 2022) in an implicit surface-atmosphere coupling (Polcher et al., 1998). Several other useful parameters are also computed, such as surface temperature ( $T_S$ ), surface albedo and emissivity, which are needed to calculate the upwelling components of the radiative budget. The calculations are performed at the grid cell scale, by aggregating its landscape into three soil tiles: one for the forest, one for grass and crops, and one for the bare soil. The aerodynamic parameters of the grid cell correspond to the averaged parameters weighted by the effective areal fraction of each soil tile.

245 The raw output data of this climate simulation have been post-processed, and only a variety of specific variables describing atmospheric ~~as well as~~ and land surface conditions have been archived for further uses. These include atmospheric variables on half-eta levels ( $M$ ) such as  $q$ , potential temperature ( $\theta$ ) and horizontal wind components ( $u$  and  $v$ ). The surface data involve ~~among others~~ skin temperature  $T_S$ ,  $SP$ , precipitation rate,  $H$  and  $LE$ , the four components of ~~radiative fluxes, as well as the~~  
250 ~~radiative budget, and~~ the underground liquid water content. The most conventional meteorological variables, such as  $T$  and  $RH$  at 2 m agl are also available. The data ~~are were~~ stored at a ~~temporal resolution of 33 for all but~~—hour temporal resolution for all variables except for the underground liquid water content. ~~More specifically, the data on half-eta levels correspond to nearly instantaneous values every~~ Specifically, the turbulent heat and radiative fluxes are 3-hour starting at 00:00—hour time-centered averages, labeled at 01:30, 04:30, 07:30, 10:30, 13:30, 16:30, 19:30 and 22:30 UTC. Meanwhile, the  
255 ~~surface data, mostly provided by ORCHIDEE, consist of time-centred mean over a 3-window and their timestamps start at 01:30~~ atmospheric variables at half-eta levels  $q_M$ ,  $u_M$  and  $v_M$ , as well as those near the surface  $T_S$ ,  $SP$ ,  $T_{2m}$  and  $RH_{2m}$ , are nearly instantaneous at 00:00, 03:00, 06:00, 09:00, 12:00, 15:00, 18:00 and 21:00 UTC. The underground water content is archived ~~at a daily timescale. It consists of liquid water height within different sub-layers, each sub-layer holding~~

daily and consists of the height of liquid water within various sublayers, each containing one node.

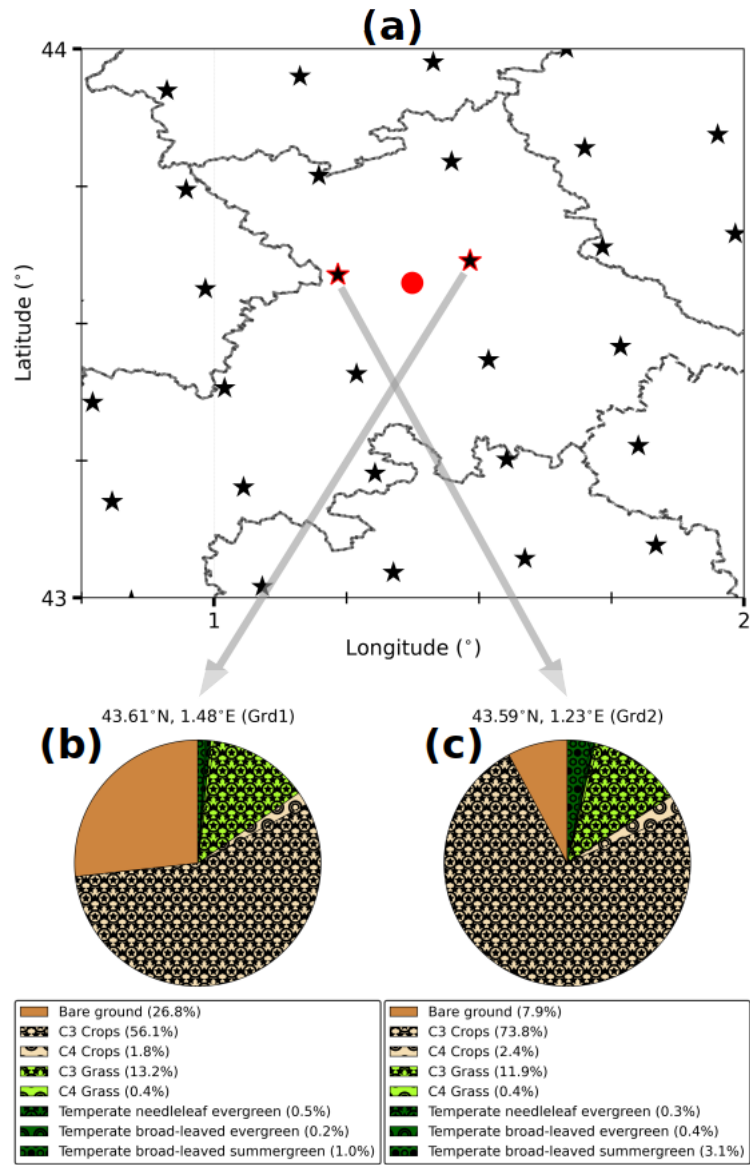


**Figure 3.** Landscape composition at the two (a) The RegIPSL grid cells-mesh (black stars) around the geographical location of the RegIPSL model-Météopole site (GrdPt red circle)geographically nearest to-. The dashed lines indicate the Météopole-flux-stationadministrative subdivisions. The two nearest grid cells (Grd1 and Grd2) are highlighted with red edges. (b) and (c) Landscape composition in these two grid cells, GrdPt+Grd1 (b) being the closest.

It would be very interesting to extract the simulation data at a grid cell with a landscape composition that resembles the landscape contribution to the turbulent heat fluxes measured at the ~~Météopole-flux station~~Météopole station, as found by Jomé et al. (2023). This grid cell should also be geographically close to the station to preserve the local behaviour of atmospheric forcing. However, for all the grid cells located within a distance 60 km to the station coordinates (e.g. 3 times the simulation horizontal resolution), at least 50 % of the surface is covered by crops and forest PFTs. The areal fraction of grass PFTs ranges between 10 – 21 %. The simulation data are then extracted at the two nearest grid cells to the Météopole site, as usually done. Figure 3 shows their landscape composition. The proportion of bare soil and crops are respectively greater and smaller in the closest grid cell (~~GrdPt~~Grd1, Figure 3b). Only the simulation covering the period from 01 January 2012 (the first year of heat fluxes measurements at the Météopole station) to 31 December 2016 is considered. This period coincides with the selected observation period from 24 November 2012. ~~The time-centred~~For consistency with radiative and heat fluxes, the time-centered average of  $q_M$ ,  $\theta_M$ ,  $u_M$  ~~and~~,  $v_M$  ~~are used for consistency with surface and soil data~~,  $T_S$ ,  $SP$ ,  $T_{2m}$  and  $RH_{2m}$  ~~are used~~. The  $SWC$  at the soil nodes is calculated as the ratio of liquid water height over the thickness of the corresponding ~~sub-layers~~sublayer. For each node, the value of  $SWC$  at a given day is assigned to every 3 hourly timestamp of that day. Similarly to the selected observational data, the days with cumulative rainfall exceeding 5 mm were excluded, reducing the simulation data by around 15 %.

### 3.3 The data-driven statistical model

Since the fluxes  $H$  and  $LE$  are continuous variables, our problem is formulated as multivariate regression settings. There are several ways to ~~achieve~~perform regression with ANNs. The easiest is to exploit the most basic ANN, the feed-forward network also known as the multi-layer perceptron (MLP). ~~Because of~~Due to its exceptional ability to approximate complex multivariate functions, MLP has become the most widely used type of ANN. Accordingly, our data-driven statistical model is built using MLP. This section begins by briefly introducing this type of ANN. Subsequently, the implementation of the statistical model with half-hourly observational data is detailed. Finally, the challenges involved in its application to ~~data from the~~the data from climate simulation are outlined.

#### 3.3.1 The multi-layer perceptron

The elementary unit of ANNs is the mathematical neuron (Rosenblatt, 1960), which is illustrated in Figure 4. It is a numerical computational unit that receives information ~~via~~through synaptic connections characterized by weights ( $w$ ), and provides a

response using an activation function ( $f$ ) and a bias ( $b$ ), as follows:

$$o = f\left(b + \sum_{j=1}^N w_j \cdot x_j\right) \quad (3)$$

Where  $N$  is the number of input variables. In general, the input data of  $f$  and its output range within  $[-1, 1]$ . The neuron's behaviour, either linear or non-linear, is defined by its activation function. Although there are many types of activation functions, sigmoid-like functions (e.g. logistic and hyperbolic tangent) and identity functions the identity function are commonly used for regression (Zhang, 2008).

295

The MLP is a supervised ANN, which consists of fully interconnected neurons organised in successive layers (see Figure 5 for illustration). This includes These layers include an input layer to receive the predictors, an output layer to get the outcome, and at least one intermediate layer between them, the so-called hidden layer(s). There is one neuron per input and output variable. The neurons in the input layer just carry the data without any calculations. The hidden layer(s) form the computational core of MLP. Although the topography of hidden layers (number of layers and neurons) has an impact on the network's capability to approximate the relationships, there is not yet a universal rule defining the most suited for a given problem. Thus, finding an appropriate configuration for hidden layers (number of layers and neurons) is generally a non-trivial and uphill task with expensive computational costs.

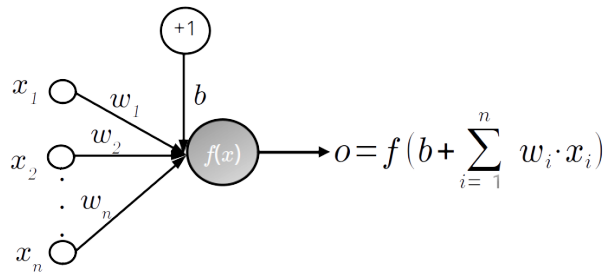


**Figure 4.** Schematic illustration of a mathematical neuron (adapted from Zhang, 2008):  $x_i$ ,  $w_i$  correspond respectively to its numerical inputs and synaptic weights, whereas  $o$  is the response based on its activation function ( $f$ ) and bias ( $b$ ). This latter is schematized by an input variable with a value and weight equal to  $+1$  and  $b$  respectively.

305

As a supervised ANN, MLP acquires knowledge about its task through a learning stage. During this stage, the network is provided with examples of paired predictors and desired outputs, and its weights and biases adjust accordingly. The MLP

understanding of the physics laws then entirely relies upon the quality and amount of data on which it has ~~learnt~~learned. Thus, the more consistent examples, the more chances of the MLP being accurate over unseen input data. The learning data is usually separated into two disjoint subsets: training and validation. The MLP weights and biases are updated using a backpropagation optimization technique which minimizes an error metric calculated on the training data, between the MLP outputs and the desired values. The Mean-Square-Error (MSE) is the common error metric (Zhang, 2008) for regression. In general, there are three modes in which backpropagation optimization may be applied: (i) the 'online' mode in which the network weights and biases are updated for each example in the training set, (ii) the 'batch' mode in which all the training data are considered at once, and (iii) the 'mini-batch' mode which is a mixture of the two first and achieves their advantages while limiting their inconveniences; the training data is subdivided into a smaller fixed number of samples (the mini-batch) which are used for modifying weights and biases. The default mini-batch size is 32. Another key parameter of the learning stage is the number of training data passages through the network, also called epochs (Chicco, 2017; Zhang, 2008; Kruse et al., 2013). Indeed, with small epochs, the network would not understand the complexity of the data, leading to an underfitting. By contrast, too high epochs may lead to overfitting; the network would capture all the details of the training data while performing badly on unknown data. The validation data serve to assess the network performance during the updating of its weights and biases. Thus, a fairly large number of epochs can be envisaged to avoid underfitting and the learning is early stopped when the performance over the validation set no longer improves, preventing overfitting.

Thus, the implementation of MLP can be split into three main points:

- (i) Define a set of relevant predictors based on the variables to be approximated.
- (ii) Select a learning data such that it would contain sufficient examples to statistically describe the relationships between predictors and targeted variables.
- (iii) Find suitable MLP setting (~~topography~~topology of hidden layer(s), activation function, etc.) through sensitivity experimentation.

Before processing with MLP, data should be scaled (i) for consistency with  $f$  and (ii) to circumvent the relevance of variables due to their magnitude. Moreover, the backpropagation algorithm is stochastic, which ~~very~~ often leads to variability in the final weights and biases of MLP each time the network is retrained with the same data. Indeed, the final state may correspond to a local minimum of the error metric (Zhang, 2008). Although the difference between the MLP outputs is usually slight, it can be ~~a-bit~~ annoying not to get the same results. The ensemble learning approach (Ganaie et al., 2022) may ~~be-used-to~~

335 limit the instability of the MLP-based estimates and ~~to~~ get closer to the optimal estimate. Instead of training a single MLP, this approach involves training multiple MLPs and then averaging their outputs for regression problems. One of the standard strategies for generating these MLPs is bagging (Breiman, 1996; Khwaja et al., 2015); a base MLP is trained on a redistributed version of the original training or learning set.

### 340 3.3.2 Implementation

In this work, each MLP is implemented using Tensorflow-Keras ~~(version 2.2.0, Abadi et al., 2016)~~ (version 2, Abadi et al., 2016), a Python library specifically designed for ANNs, known for its user-friendly interface. Unless otherwise mentioned, the default parameters are used. The three points mentioned above are addressed as follows:

– (i) As MLP predictors, we ~~looked for standardized use 13~~ variables that can be derived from ~~both observational and modelled observational and simulation~~ data while still having the same physical meaning. ~~Theoretically~~ Their formulations are shown in Table 2. Indeed,  $H$  and  $LE$  are theoretically quasi-constant within the surface layer and strongly related to near-surface radiative, thermodynamic, and dynamical forcing. Moreover, their relative predominance is controlled by the wetness of the uppermost part of the soil. In numerical simulations, the atmospheric level just above the ground is usually ~~considered to be~~ the top of the surface layer. ~~Based on~~ Therefore, considering the observed variables in Table 1 and the ~~simulation variables~~ variables from the simulation that have been archived, we ~~derive~~ derived a set of 9 physical variables that may analogously ~~describe~~ summarize the environmental forcing in the surface layer. ~~These include the total energy governing the~~ They include the radiative energy governing surface processes ( $R_{net}$ ), the meteorological conditions in the surface layer ( $\theta_{sl}$ ,  $\Delta\theta$ ,  $q_{sl}$ ,  $\Delta q$ ,  $u_{sl}$ ,  $v_{sl}$ ,  $\Delta U$ ) and the moisture in the uppermost soil layer ( $SM$ ). Eventually, 4 trigonometric temporal coordinates are added ~~for the description of~~ to describe seasonal ( $d_x$ ,  $d_y$ ) and diurnal ( $h_x$ ,  $h_y$ ) cycles. ~~The formulations of all these 13 variables, used as MLP predictors, are presented in Table 2.~~ Under the observed environment,  $SM$  is defined by  $SWC_{-10cm}$  (the first depth of soil moisture measurements) and the meteorological variables are calculated assuming that the surface layer always extends above 10 magl. ~~Under~~ For the simulated environment,  $SM$  then corresponds to  $SWC_{-12.3cm}$  (the nearest node to the measurement depth). ~~Moreover~~ Diagnostic variables derived from numerical simulation ( $T_{2m}$ ,  $RH_{2m}$ ) are susceptible to contain bias due to the interpolation technique and the inconsistency of terrain elevation. To avoid these uncertainties, the meteorological variables are ~~directly taken~~ taken directly at the first half-eta level ( $M=1$ , around 8 magl) ~~instead of diagnostic variables~~ as much as possible. In both observed and simulated environments,  $\Delta U$  is calculated assuming a null horizontal wind



speed at the ground. Due to ~~the~~ missing data, the sunrise hour required to compute  $h_x$  and  $h_y$  was retrieved using the astral package (version 3.0), and rounded to the nearest half hour.

- 365 – (ii) To train the statistical model over as many multivariate cases as possible, the half-hour observational data from the five most covered years (Figure 2) were gathered as the learning set. The remaining data was reserved for assessing its ability to generalize, it will be referred to as the test set.
- (iii) Since  $H$  and  $LE$  are complementary fluxes and to avoid excessive sensitivity experiments in the search for a relevant architecture for MLP, the neurons in the output layer were set to 2, one for each flux. Following the literature (Kumar et al., 2011; Leufen and Schädler, 2019; Kelley and Pardyjak, 2019; Kelley et al., 2020), hyperbolic tangent and identical  
370 functions were used as the activation functions for neurons of the hidden and output layers, respectively. The weights and biases optimization was carried out with the Adam-amsgrad backpropagation algorithm (Kingma and Ba, 2017; Reddi et al., 2018) in a default mini-batch mode, and MSE was chosen as the error to minimize. Based on preliminary results, we opted for the same strategy of network training used by Leufen and Schädler (2019). The network update stops at  
375 most after 1000 epochs. Otherwise, the update is stopped early if the MSE on the validation data does not improve after 50 successive epochs, and then the network state is finally set to the epoch with the best MSE.

The input and output data are scaled to the interval  $[0, 1]$  similarly to Leufen and Schädler (2019) as follows:

$$\tilde{x} = \frac{x - x_{min}}{x_{max} - x_{min}} \quad (4)$$

~~Where~~ where  $x_{min}$  and  $x_{max}$  correspond to the extreme values ~~of variable  $x$~~ . They are set to the theoretical values of the  
380 trigonometric functions (e.g.,  $-1$  and  $1$  respectively) for the four temporal coordinates. For the other nine physical parameters, these values are set ~~such~~ so that the resulting interval strictly holds both the observational and RegIPSL data (see Figure A1).

The MLP base architecture used in this study ~~includes~~ involves two hidden layers with 4 and 3 neurons, respectively (Figure 5). It was found through several series of sensitivity experiments ~~using the learning data with the learning set~~ (not shown). A  
385 bagging-based strategy was used to ~~incorporate the account for the strong~~ inter-annual variability of  $H$  and  $LE$  ~~when building the statistical model in their statistically-based estimates~~. Indeed, a 5-fold cross-validation (Andersen and Martinez, 1999) with year-wise data splitting was applied to the learning data set to generate 55 bagged MLPs, ~~such that the statistically-based fluxes are the average across the individual MLP outputs~~. Cyclically, the data from one year were used as the validation data set whilst the others composed the training dataset, and, 11 MLPs were trained by randomly initializing weights and

**Table 2.** The 13 MLP input variables, derived from observational data and their equivalent extracted from RegIPSL data.  $dd$ ,  $\Delta h$  and  $N_y$  included in the expressions of the temporal coordinates ~~respectively~~ stand for are the Julian date, hours relative to sunrise on  $dd$  and number of days in the year.

Observations	RegIPSL
Radiative forcing at the surface	
$R_{net}$	$R_{net}$
Thermodynamic and dynamic in the surface layer	
<ul style="list-style-type: none"> <li><math>\theta_{sl} = \frac{\theta_{10m} + \theta_{2m}}{2} ; \Delta\theta = \frac{\Delta\theta}{\Delta z} \Big _{2m}^{10m}</math></li> <li><math>q_{sl} = \frac{q_{10m} + q_{2m}}{2} ; \Delta q = \frac{\Delta q}{\Delta z} \Big _{2m}^{10m}</math></li> <li><math>[u, v]_{sl} = [u, v]_{3.7m} ; \Delta U = \frac{\Delta U}{\Delta z} \Big _{surface}^{3.7m}</math></li> </ul>	<ul style="list-style-type: none"> <li><math>\theta_{sl} = \theta_{M=1} ; \Delta\theta = \frac{\Delta\theta}{\Delta z} \Big _{surface}^{M=1}</math></li> <li><math>q_{sl} = q_{M=1} ; \Delta q = \frac{\Delta q}{\Delta z} \Big _{2m}^{M=1}</math></li> <li><math>[u, v]_{sl} = [u, v]_{M=1} ; \Delta U = \frac{\Delta U}{\Delta z} \Big _{surface}^{M=1}</math></li> </ul>
Underlying soil wetness	
$SM = SWC_{-10cm}$	$SM = SWC_{-12.3cm}$
Temporal coordinates	
<ul style="list-style-type: none"> <li><math>d_x = \cos(2\pi \cdot \frac{dd}{N_y}) ; d_y = \sin(2\pi \cdot \frac{dd}{N_y})</math></li> <li><math>h_x = \cos(2\pi \cdot \frac{\Delta h}{24}) ; h_y = \sin(2\pi \cdot \frac{\Delta h}{24})</math></li> </ul>	<ul style="list-style-type: none"> <li><math>d_x ; d_y</math></li> <li><math>h_x ; h_y</math></li> </ul>

biases along with a shuffling of the training data before composing mini-batch subsets. ThusIn this way, each example in the learning data-set was at least once used as validation or training data. ~~Although this number of~~ Even though the number 11 was arbitrarily chosen ~~following based on~~ the available computing resources, it ensures the repeatability of ~~the estimates.~~ Thus, the statistically-based estimates of observed fluxes are the average across the individual MLP outputs. In the following, we refer to these as MLP-based fluxes or estimates.

395

### 3.3.3 Application to data from numerical model

~~The key objective of our evaluation method is to approximate turbulent heat fluxes that may be observed under modelled environmental forcing using an MLP-based statistical model built with observational data . This implicitly assumes that the~~

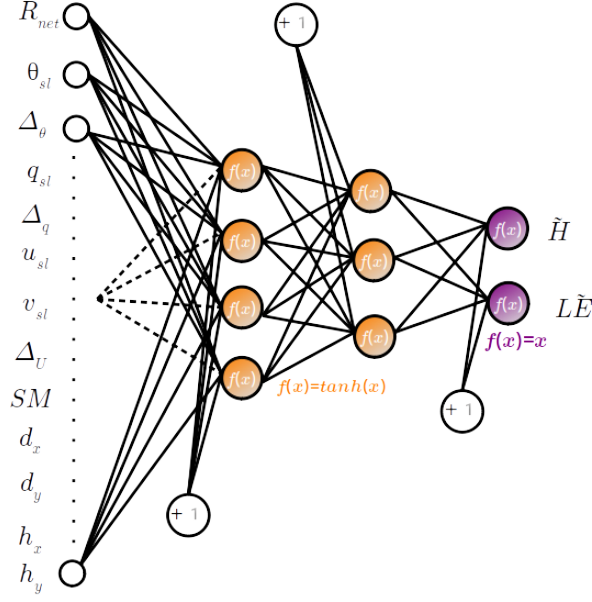


**Figure 5.** Architecture of MLP used in this study. The input variables are described in table 2.

400 ~~modelled and observed data~~ model is built using half-hour observational data to take advantage of more samples. After that, it will be applied to the 3-hour simulation data to provide  $H$  and  $LE$  that are likely to be observed in the simulated environment. This assumes that simulated and observed environments share a common ~~input space and that space~~, and the learning data is representative of this space. However, if the model data do represents that space. On one hand, the difference in temporal resolution could introduce artificial errors that might impact both the statistical model's performance and comparison results.

405 These potential impacts are discussed at the beginning of section 5. On the other hand, if the simulated environment does not have similar structures (distribution and interval ranges of input variables) to the observations, the statistical model may ~~poorly perform~~ perform poorly. Indeed, MLP has a good interpolation capability, but may not ~~extrapolate well~~ correctly extrapolate beyond the ranges of values it has ~~learnt on~~ (Bonnasse-Gahot, 2022). For ~~learned~~ (Bonnasse-Gahot, 2022). Yet, for four of the nine physical variables ( $\Delta_\theta$ ,  $\Delta_q$ ,  $u_{sl}$  and  $v_{sl}$ ) ~~RegIPSL~~ the simulation data spread beyond the observed values (Figure A1).

410 A rigorous application of machine learning techniques ~~typically~~ requires the use of transfer learning to mitigate ~~the loss of performance~~ performance loss when trained ANN is applied to data originating from another source (Day and Khoshgoftaar, 2017). Since the observed  $H$  and  $LE$  associated with the ~~modelled~~ simulated environment are unknown, the most challenging transfer learning approach, unsupervised domain adaptation, would normally be used in our case. Numerous methods are available for achieving unsupervised domain adaptation. We tried the easiest and most popular methods over the ~~RegIPSL~~

415 ~~input data~~ simulation input data, such that correlation alignment (Sun et al., 2015), feature augmentation (Daumé III, 2009),

subspace alignment (Fernando et al., 2013), transfer component analysis (Pan et al., 2011) and feature selection (Uguroglu and Carbonell, 2011) as implemented in ADAPT library (version 0.4.2, de Mathelin et al., 2023). Either, we get unreasonable fluxes, particularly in stable conditions, or the fluxes vary from one method to another, so it is hard to conclude the most effieient suitable. The most sophisticated methods require the use of an encoder, which may be an ANN, with the laborious and time-consuming task to find its adequate of finding its appropriate configuration. Further investigation is investigations are then needed to find a consistent suited unsupervised domain adaptation method, but that is beyond the scope of this paper.

Finally At this stage, our proposed evaluation method does not currently yet include any transfer learning method. Under the traditional assumption that training and testing data come from the same distribution and input space (Aggarwal, 2014), the MLP-based statistical model is directly applied to RegIPSL input data. To get an insight into the loss of performancee simulation data. Nonetheless, to gain insight into performance loss, the relative contribution of predictors towards the fluxes each predictor to flux estimates is calculated using the SHapley Additive exPlanations (SHAP) algorithm (Lundberg and Lee, 2017). SHAP is attractive because it unifies several common methods for interpreting the approximation with ANN. It is based on the game theory approach; for an individual game (MLP outputs), contributions (called SHAP values) are assigned to each player (predictor). The mean of average of the SHAP absolute value across in several instances is then used to measure the predictor influence. The higher the corresponding SHAP value, the more contributing the input variable contributes on average.

#### 4 Assessment of Assessing the data-driven statistical model

As mentioned above, the data-driven model consists previously, the MLP-based  $H$  and  $LE$  are the average over the outputs of 55 MLPs that were trained under a 5-fold cross-validation applied to a collection of 5 years of observational data. The estimated fluxes are then the average of their outputs. The most important goal trained with the learning set. The key objective in machine learning is generalization, e.g. which means that the data-driven model should perform well not only on learning data but also on unseen data under known and unknown conditions. This section discusses the performance of our statistical model on learning and test sets.

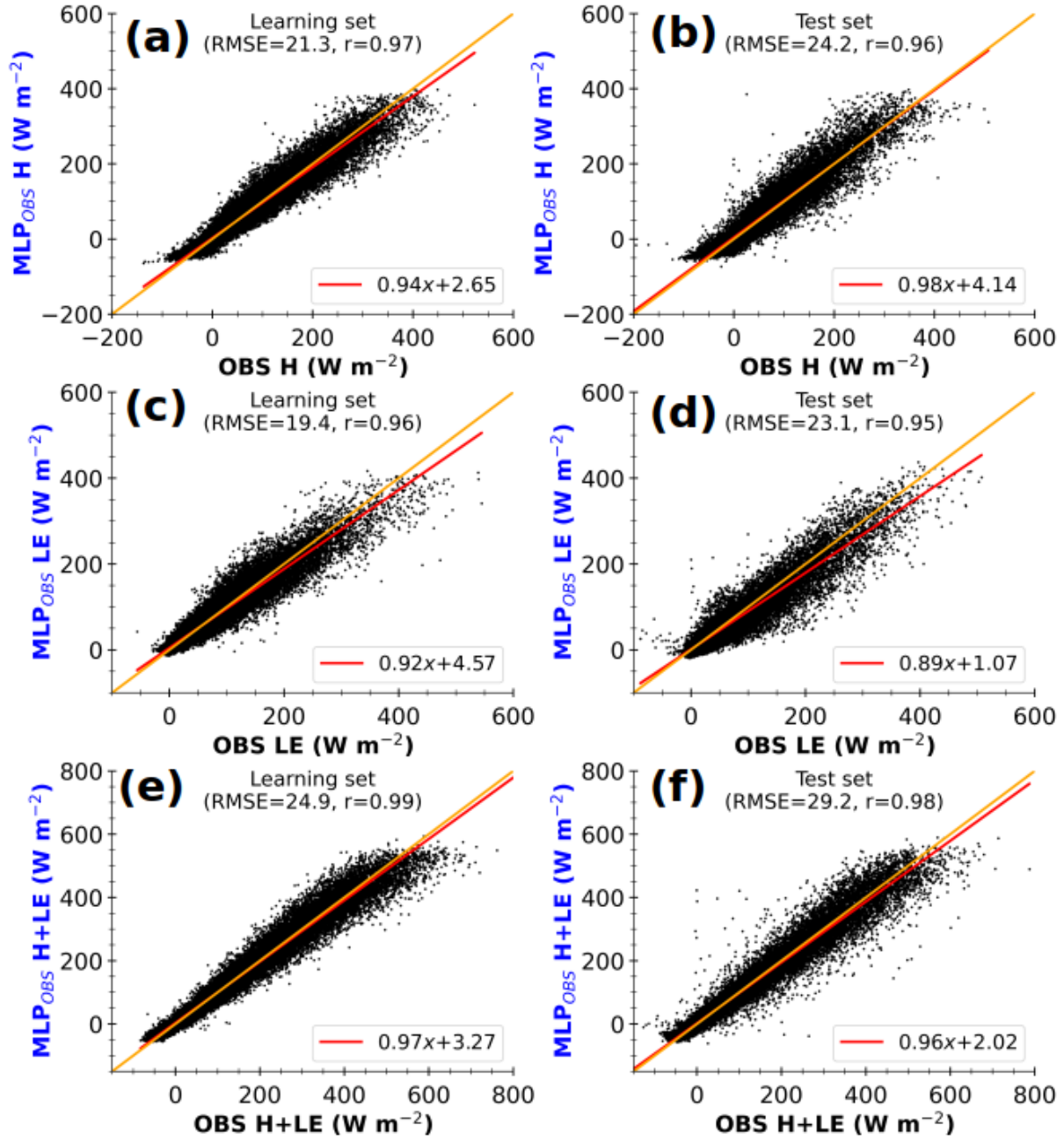


**Figure 6.** Half-hourly statistical-estimates (MLP-based) estimates of observed sensible heat flux ( $MLP_{OBS} H$ , a and b), latent heat flux ( $MLP_{OBS} LE$ , c and d) and total turbulent heat flux ( $MLP_{OBS} H + LE$ , e and f) with observed input data against observed fluxes ( $OBS$ ), for learning (a, c and e) and test (b, d and f) sets. The values at the top of each panel correspond to Root-Mean-Square Error (RMSE) and Pearson's correlation coefficient. The lines in magenta-red and orange represent the linear regression and identical fits, respectively. The axis labels are colored according to the schematic illustration in Figure 1 (right side).

Figure 6 compares half-hourly MLP-based fluxes ~~against their targeted values~~ ( $MLP_{OBS}$ ) ~~against their observed values~~ ( $OBS$ ), for learning and test sets ~~separately~~ (left and right panels, respectively). It shows  $H$  and  $LE$  (top and middle panels respectively) and the total turbulent heat flux  $H + LE$  (bottom panels). Overall, the ~~root-mean-square-error~~ ~~root-mean-square-errors~~ (RMSE) range between  $2030 \text{ Wm}^{-2}$  and the Pearson's correlation ~~coefficient~~ ~~coefficients~~ ( $r$ ) are greater than 0.95, indicating ~~a very good~~ ~~an excellent~~ agreement between estimated and observed fluxes. Interestingly, ~~the total turbulent heat flux~~  $H + LE$  is particularly well approximated, despite not being a direct output of MLPs. Furthermore, the RMSE increases by less than ~~320%~~ and the correlation is almost the same from learning to test sets. ~~Thus, on both known learning data and unknown test data~~ ~~data~~. Hence, under both known and unknown observed conditions, the statistical model

445 performs quite similarly on average, demonstrating ~~that it generalizes rather well~~ ~~a fairly good generalization ability~~. Besides this ~~remarkable performance, there are good performance~~, some noticeable shortcomings ~~shown in both~~ ~~appear in both the~~ learning and test sets. On the one hand, ~~the estimated~~  $MLP_{OBS} H$  is ~~limited to around~~ ~~bound to about~~  $-50 \text{ Wm}^{-2}$  ~~while values of less than~~, while values below  $-100 \text{ Wm}^{-2}$  are observed (Figure 6a and b). On the other hand, ~~the~~  $MLP_{OBS} LE$  ~~tends to underestimate~~ observed  $LE$  ~~greater than above~~  $200 \text{ Wm}^{-2}$  ~~tends to be underestimated~~ (Figure 6c and d), es-

455 pecially for the test set. ~~Thus, This indicates that the statistical model has issues with estimating~~ ~~struggles to estimate~~ large  $LE$  and negative  $H$  ~~associated with a very~~, which are associated with highly unstable and stable surface layer regimes, respectively.

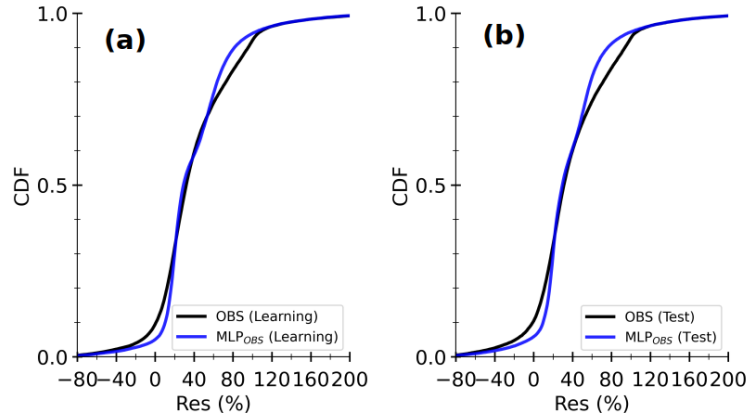


**Figure 7.** Cumulative density functions (CDFs) of RES (eq. 2) calculated with half-hourly observed turbulent heat fluxes ( $OBS$ , in black) and competing MLP-based estimates ~~with observed input data~~ ( $MLP_{OBS}$  in blue) for learning set (a) and test set (b) in Figure 6.

Figure 7 shows the cumulative distribution functions (CDFs) of  $RES - RES$  (eq. 2) calculated with half-hourly observed  $R_{net} - G$  together with observed and MLP-based  $OBS$  and  $MLP_{OBS}$  fluxes. For both learning and test sets (Figure 7 a and b resp.), CDFs of observed fluxes and estimated fluxes nearly coincide  $OBS$  and  $MLP_{OBS}$  are close but the MLP underestimates the strong (negative or positive)  $RES$  values. Although the sample size is different for these two sets, their CDF curves look quite similar, implying that they are individually representative of the main local characteristics of energy imbalance and that the statistical model reproduces quite well. Closer inspection showed that the statistical model produces provides smoothed fluxes that preserve the observed relationship between striking relationship between  $OBS$   $H + LE$  and  $R_{net} - G$  (not shown). This smoothing is the main cause of intermittent departures between the CDF curves. Overall, the CDFs are smaller than 0.25-0.15 for  $RES$  lower than 20 % indicating that both observed and estimated  $OBS$   $H + LE$  and  $MLP_{OBS}$   $H + LE$  are smaller than  $R_{net} - G$  in most of the the majority of cases. This tendency is systematic for large  $H + LE$  (not shown). Thus, the statistical model carries the limitations of observed turbulent heat fluxes. The representativity of local measurements representativeness of turbulent heat fluxes in heterogeneous landscapes with the EC technique is being investigated measured at the permanent Météopole site on the coarser horizontal scale of numerical models is being examined as part of the MOSAI project (e.g. Jomé et al., 2023).

Table 3 compares RMSE,  $r$  and coefficients of the linear regression (slope and intercept) when the statistical model is applied to the half-hourly raw observational data (in Figure 6) and 3-hourly averaged values similarly to RegIPSL data. It provides insights into the performance at the temporal resolution of simulation data. The values of these metrics show that the statistical model performs better at the temporal resolution of 3-

Comparison of Root-Mean-Square-Error, linear correlation and the linear regression fitting coefficients (slope and intercept) when applying the MPL-based statistical model to half-hourly raw and to 3-hourly average observational data. The statistical model has been constructed using the half-hourly version of the learning set (Figure 2a):

	$H - LE$	$H + LE$	$H - LE$	$H + LE$
30	21.9	20.4	25.9	25.2
24	2	30.8	3	17.6
16	5	16.1	20.7	19.3
20	7	19.3	20.7	19.3
0.98	0.97	0.99	0.96	0.95
0.98	0.97	0.99	0.97	0.97
0.94	0.91	0.97	0.98	0.89
0.96	0.93	0.99	1.01	0.91
0.98	0.98	0.98	0.98	0.98
3	3.56	5.46	4.22	5.77
1.29	3.43	3	1.44	4.96
1.51	3.50	0.70	0.38	

Figure 8 shows the composite seasonal cycles of observed and MLP-based turbulent heat  $OBS$  and  $MLP_{OBS}$  fluxes for the learning and test sets (left and right panels, respectively). The observed  $H + LE$  presents quite similar seasonal cycles for both

sets, with a peak from April to September (Figure 8c and f). However, observed  $H$  and  $LE$  do not typically present the same seasonal cycle. Indeed, from April to September,  $H$  ( $LE$ ) is on average stronger (weaker) in the learning set ~~than in~~  
490 ~~the test one. In the learning~~ set,  $LE$  predominates over  $H$  from March to June ~~and it is the reverse in the subsequent months~~  
~~until~~, ~~with the reverse occurring from July to~~ October (Figure 8a and b). ~~In~~ ~~Whereas in~~ the test set, the predominance of  $H$   
starts later in August, since  $LE$  slowly decreases from May to July (Figure 8d and e). ~~This highlights the~~ ~~The~~ inter-annual  
variability ~~in the partitioning of turbulent fluxes across the period from late spring to late summer, as shown presented in~~  
Figure A2 ~~, that explains this disparity. Indeed, the year 2022 presents a seasonal cycle that differs from the one of other years,~~  
495 ~~which~~ different vegetation dynamics, ~~driven by different atmospheric conditions,~~ may explain. ~~This highlights the importance~~  
~~of covering several annual cycles to well train the MLPs.~~

Overall, the ~~MLP-based~~  $MLP_{OBS}$  fluxes correctly reproduce the observed ~~signal of~~ seasonal cycles along with day-to-day  
variability for both learning and test sets. This is particularly true for the total turbulent heat flux (Figure 8c and f). Interestingly,  
500 the relative predominance between  $H$  and  $LE$  ~~in the two sets~~ is remarkably well replicated ~~in the two sets~~. In the learning  
set, the absolute difference between estimated and observed fluxes remains smaller than  $5 \text{ Wm}^{-2}$  for all the fluxes. However,  
in the test set, striking differences appear between May and September, when the total turbulent heat flux is at its maximum.  
Indeed, while the ~~MLP-based~~  $MLP_{OBS}$   $H + LE$  is quite similar to observations (Figure 8f), the ~~MLP-based~~  $MLP_{OBS}$   
 $H$  overestimates observations (Figure 8d), by more than  $10 \text{ Wm}^{-2}$  in June and July, and, the ~~MLP-based~~  $MLP_{OBS}$   $LE$   
505 underestimates observations, by more than  $14 \text{ Wm}^{-2}$  from July to September (Figure 8e). This ~~likely~~ comes from the fact that  
the MLPs have ~~learnt on~~ ~~learned~~ respectively weaker  $LE$  and stronger  $H$  on average (Figures 8 and A2).

In conclusion, the statistical model, constructed with half-hourly observational data, provides highly consistent estimates of  
510 ~~observed~~  $H$  and  $LE$ . It especially approximates ~~very quite~~ well the total ~~turbulent heat~~ flux  $H + LE$ . ~~The non-closure of SEB~~  
~~embedded in the observed fluxes is also reproduced, but lightly reduced for the strongest values.~~ Its performance in terms of  
RMSE and linear correlation ranges within the best reported by the literature on surface parametrization schemes (e.g. Liu  
et al., 2013; Leufen and Schädler, 2019; Román-Cascón et al., 2021). ~~The non-closure of SEB embedded in the observed fluxes~~  
~~is also replicated. The performance improves considerably at 3-hour and seasonal timescales, probably due to a reduction~~  
515 ~~of noise in the observational data.~~ In particular, the relative predominance between heating and evaporation is faithfully  
reproduced ~~. All these results underlie that the statistical model captured rather well the fundamental~~ ~~at the seasonal scale.~~



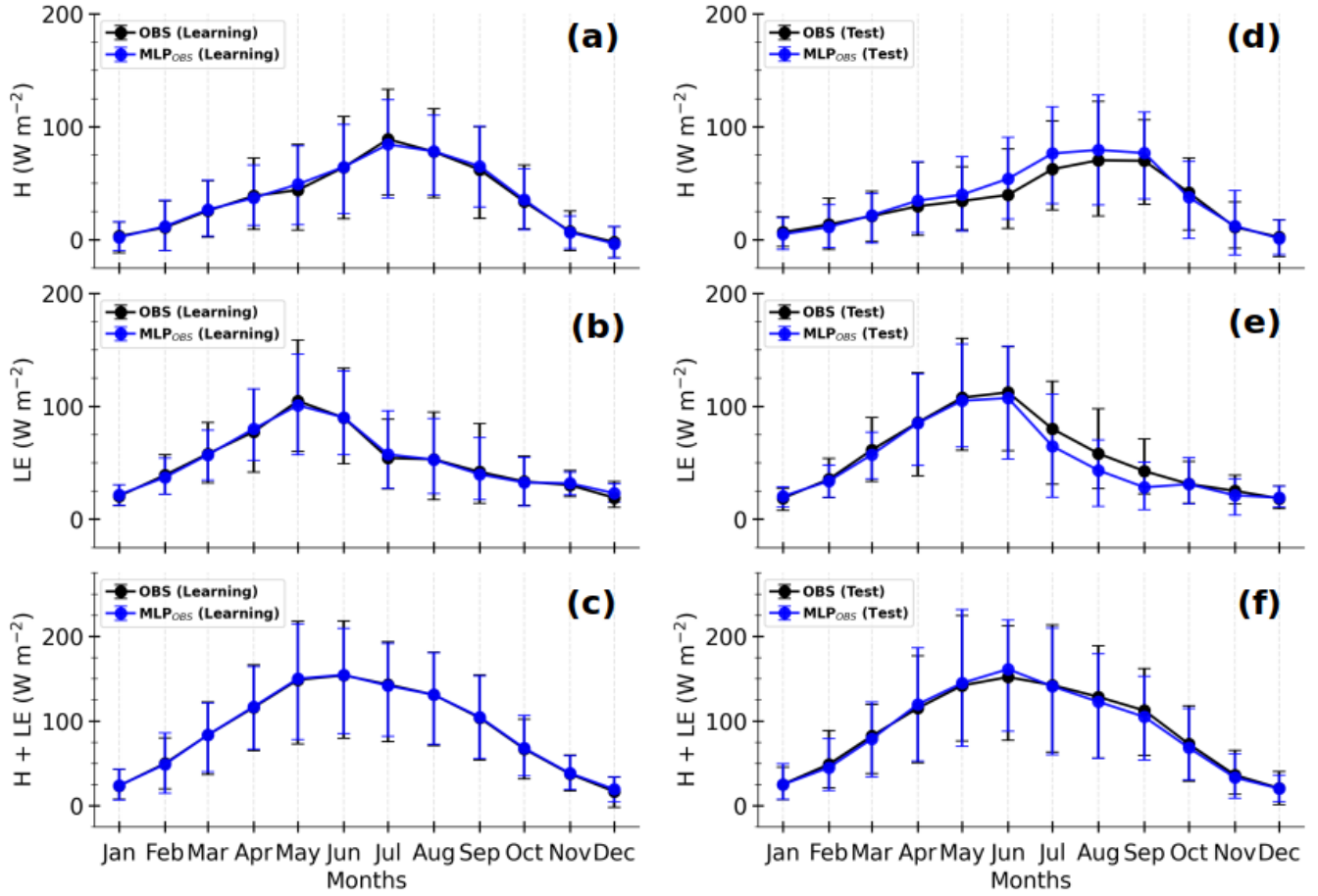


**Figure 8.** Composite monthly average-averages of observed and (OBS in black) and MLP-based (MLP<sub>OBS</sub> in blue) sensible heat flux ( $H$ , a and d), latent heat flux ( $LE$ , b and e) and total turbulent heat flux ( $H + LE$ , c and f) observed and statistically-estimated-with-input-observed data (lines in black and cyan respectively) for the learning and test sets (left and right panels, respectively). The solid lines represent the means and the error bars correspond to 10<sup>th</sup>-10<sup>th</sup> and 90<sup>th</sup>-90<sup>th</sup> percentiles, calculated by gathering the daily averages of half-hourly samples in Figure 6.

The most fundamental local links between turbulent heat-fluxes and environmental factors seem to be well captured by the data-driven model. However, the statistical model shows limitations in estimating a very it shows limitations with estimating large  $LE$  and negative  $H$ , notably at hourly timescale. Moreover, it struggles to generalize the magnitude of  $H$  and  $LE$  and does not well generalize in the spring and summer seasons. Indeed months. Likely, the limited number of examples samples in the learning set does not cover all the and/or the MLP input variables do not fully convey the strong inter-annual variability of turbulent heat fluxes.

Increasing the learning data at the expense of the test data ~~would no doubt improve the skill~~ does not noticeably improve the  
525 generalization ability of the statistical model ~~on observed fluxes. However~~ (not shown). Moreover, uncertainties will always  
remain when ~~it the statistical model~~ is applied to unseen data and cannot be assessed in the absence of corresponding observa-  
tions, as is the case for numerical ~~modelssimulations~~. By convention, ~~thirty years~~ 30 years of observational data ~~are is~~ required  
for good climatological coverage ~~while around ten years is~~, while around 10 years are currently available at the ~~Météopole-flux~~  
~~station~~ Météopole permanent site. The spring and summer seasons are usually characterized by intense vegetation activity.  
530 ~~Furthermore~~ Moreover, the relationship between ~~near-surface~~ surface latent heat flux and soil moisture could be modulated by  
the ~~vegetation state (e.g. Román-Cascón et al., 2020).~~ state of the vegetation (e.g. Román-Cascón et al., 2020). However,  
the MLP input variables lack ~~one variable that can characterize the dynamics of the vegetation~~ a key factor that could capture  
vegetation dynamics, such as the leaf area index (LAI). ~~Such a parameter will then contribute to a more accurate LAI.~~  
Adding such a parameter to the input variables would provide a more robust description of the ~~inter-annual variability of~~  
535 ~~the near-surface annual variability of surface~~ turbulent heat fluxes. Hence, its use would probably improve This is likely to  
enhance the generalization ability of the statistical model, especially during the spring and summer seasons.

## 5 ~~Evaluation of Using the data-driven statistical model to evaluate~~ simulated ~~near-surface~~ surface turbulent heat fluxes ~~using the statistical model~~

540 ~~In this section, the near-surface~~ The simulated surface turbulent heat fluxes ~~simulated by the RegIPSL model,~~ from 01 January  
2012 to 31 December 2016, ~~are evaluated by focusing on the weaknesses of its land surface scheme by the RegIPSL model,~~  
are evaluated in this section. The benefits ~~and limitations~~ of our proposed evaluation approach ~~are emphasized,~~ compared to  
the traditional direct comparison between observed and simulated time series, are discussed.

545 For as much consistency as possible with the archived simulation data, 3- hour 'adapted' observational data (*OBS'*, 15739  
samples in total from November 2012 to December 2022) were derived from half-hour observations (see Table 1). Indeed,  
*SWC*, *H*, *LE* and the four radiative fluxes were time-centered averaged on a 3 –hr window, to get the same timestamps.  
The timestamp is excluded when more than half of the expected half-hour data (e.g., 3 out of 6) are missing. Half-hour data at  
these timestamps are used directly when available for the other variables (*T*, *RH*, *SP*, *u*, and *v*). If not available, *T*, *RH*, and  
550 *SP* values are obtained through linear interpolation, while *u* and *v* are taken from the nearest half-hour. First, the sensitivity of  
the data-driven model's performance to changes in temporal resolution and the effects of simulated data extending beyond the

learning range is assessed. Then, the data-driven model is applied to evaluate the simulated heat fluxes over the common period.

5.1 Impact of temporal resolution and extrapolation on flux estimates using the data-driven model

555 Table 3 shows the RMSE, r, and linear regression coefficients (slope and intercept) obtained when all  $MLP_{OBS}$   $H$  and  $LE$  from November 2012 to December 2022 are compared with their target values, for both the adapted 3 hour OBS' and the half-hour OBS from which OBS' was derived. Figure 9 shows their composite diurnal cycles, for the sub-periods during which the fluxes are weaker (November, December, January, and February), stronger with a predominance of  $LE$  (March, April, May, and June) and stronger with a predominance of  $H$  (July, August, September, and October). RMSE of  $MLP_{OBS'}$  improves by 4  $Wm^2$  data, and the other parameters in Table 3 remain the same, between OBS and OBS' datasets. The composite diurnal cycles of the observed fluxes and the MLP-based estimates for both temporal resolutions align closely with each other. This indicates that the mismatches between half-hour and coarser 3-hour time resolutions do not significantly affect the performance of the statistical model.

**Table 3.** Comparison of Root-Mean-Square-Error, linear correlation and the linear regression fitting coefficients (slope and intercept) when applying the MPL-based statistical model to half-hour raw and to 3-hour average observational data. The statistical model has been constructed using the half-hour sampling of the learning set (Figure 2a).

		$H$	$LE$
RMSE ( $Wm^{-2}$ )	half-hour	22.1	20.5
	3-hour	17.8	16.6
Correlation	half-hour	0.97	0.96
	3-hour	0.97	0.97
Slope	half-hour	0.95	0.91
	3-hour	0.97	0.93
Intercept	half-hour	2.98	2.98
	3-hour	1.71	1.68

565

Figure 10 presents the means-averages of SHAP absolute value for each input variable, averaged across the trained MLPs and the estimates under observed (, for the MPL-based  $H$  and  $LE$  for learning and test sets (in Figure 6) and simulated (at the two nearest grid-cells) environments environments at Grd1 and Grd2. The variables are ranked on the  $y$ -axis in descending order according to their relevance-at-GrdPt values at Grd1, the closest-nearest geographical grid cell. Note that, the SHAP

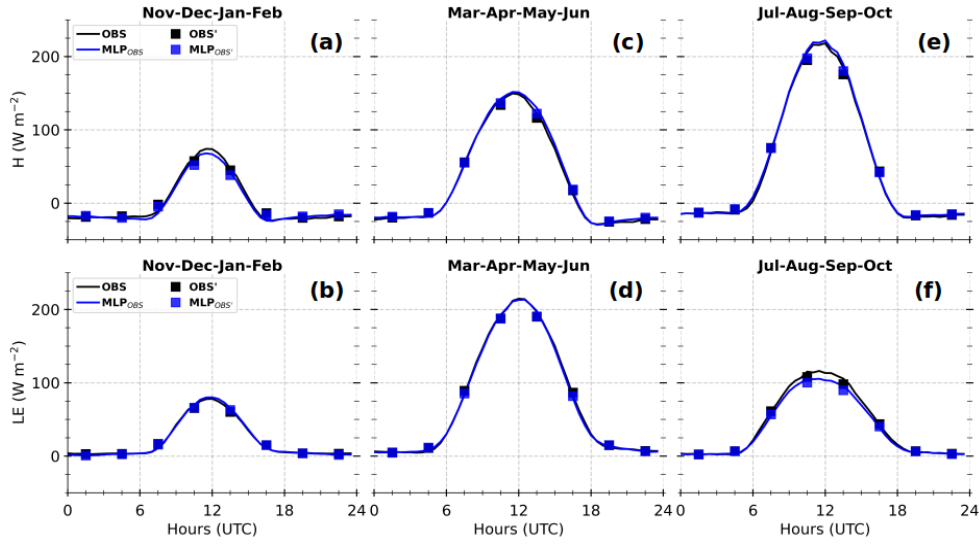


**Figure 9.** Averages of SHAP absolute-value for each input-variable in statistical-estimates. Composite diurnal cycles of sensible half-hour and 3-hour observed heat flux-fluxes ( $H$ , a OBS and OBS' in black) and latent heat flux-their competing MLP-based estimates ( $LE$  MLP<sub>OBS</sub> and MLP<sub>OBS'</sub> respectively, bin blue) under the simulated environment at GrdPt1 and GrdPt2 and, under observed learning for  $H$  (top panels) and test-sets  $LE$  (bottom panels), according to by splitting the caption. For a given MLP, annual cycle into 3 typical sub-periods (see the SHAP absolute-values are calculated-text for each estimate and then averaged over the samples of each data set. The coloured bars indicate the median values and the error bars correspond to the 10<sup>th</sup> and 90<sup>th</sup> percentiles across the 55 trained MLPs that compose the statistical model more details). In each panel, the input-variables They are ranked in descending order under the environment calculated based on diurnal cycles where at GrdPt1 least 6 out of 8 expected OBS' are available (approximately 85% of all selected diurnal cycles).

570 value increases with the variable relative contribution of the input variable. Thus, the possible loss of performance this figure allows for discussion of performance loss due to extrapolation, e.g., when the input data ranges extends beyond the learning interval could be discussed.

575 In both the observed and simulated environments Regardless of the environment,  $R_{net}$  is by far the major contributing variable. most contributing variable, followed by  $SM$  and  $\theta_{sl}$  is the third most contributing physical variable in for both  $H$  and  $LE$  estimates, regardless of the environment. The importance of the other inputs varies with the environment, the grid cells and the fluxes. Nonetheless,  $SM$  is always among the four leading physical variables. Thus, the trained MLPs composing the statistical model clearly understood that the net radiative budget at the surface is the primary driver of turbulent heat fluxes and that the soil wetness is a crucial factor for the partitioning between heating and evaporation. The contribution of  $\Delta\theta$  in the simulated environment considerably This probably explains the better agreement between observed and MLP<sub>OBS</sub> at coarser

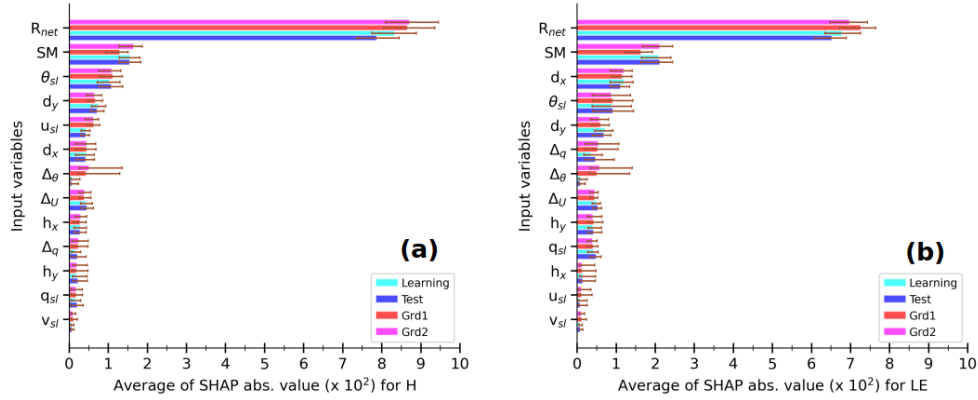


**Figure 10.** Averages of SHAP absolute value for each input variable in MLP-based estimates of  $H$  (a) and  $LE$  (b) within the simulated environment at Grd1 and Grd2, and the observed environment of learning and test sets, according to the caption. For a given MLP, the SHAP absolute values are calculated for each estimate and then averaged over the samples of each data set. The colored bars indicate the median values, and the error bars correspond to the minimum and maximum values across the 55 trained MLPs that compose the statistical model. In each panel, the input variables are ranked in descending order under the simulated environment at Grd1.

time-scales, seasonal and 3-hr, since the noise in the observational data is reduced. The importance of the other variables varies with the trained MLPs. Moreover, it is the second most contributing variable for  $H$  estimates in this environment. Whereas environment, the grid cells and the fluxes. Notably,  $\Delta_\theta$  is one of the less influential variables in the observed conditions least influential variables under observed conditions, unlike in the simulated environment. This demonstrates that the statistical model considers the change in the environmental context. Under the simulated conditions, the contribution of  $\Delta_\theta$  is quite comparable to that of  $SM$  and  $\theta_{sl}$ . Thus takes into consideration changing environmental contexts. Overall, the aggregated contribution of the three physical variables ( $\Delta_\theta$ ,  $u_{sl}$  and  $v_{sl}$ ) whose simulated values spread beyond the learning interval is overall smaller than 20 % of the aggregated contribution of  $R_{net}$ ,  $SM$  and  $\theta_{sl}$ . Therefore, we hypothesise a minor

590 hypothesize a modest loss of performance due to extrapolation when the statistical model is directly applied to data from the RegIPSL model.

## 5.2 Evaluating the simulated heat fluxes using the data-driven model

Remember that MLP-based fluxes are approximations of observed fluxes in a given environmental forcing (see section 4). When applied to simulation, they correspond to the fluxes that would have been measured if the simulated conditions were effectively observed. In the following, OBS' data (e.g., 3-hour time-centered averages) are used as observed conditions. They

are referred to as OBS for simplicity.

The scatter plots in Figure 11 illustrate the consistency of the MLP-based fluxes in the simulated environment ~~as well as the~~  
600 ~~errors due to different~~. They also highlight errors resulting from disparities in observed and simulated environmental forcing.  
It compares 3-hourly MLP-based fluxes with environmental conditions at GrdPtGrd1 ( $MLP_{Grd1}$ ) against the corresponding  
~~3-hourly time-centred average of observed fluxes~~ ( $OBS$  left panels) and MLP-based fluxes in ~~corresponding~~  
observed conditions ( $MLP_{OBS}$ , right panels). It only includes the timestamps between 24 November 2012 to 31 December  
2016 for which both ~~modelled and corresponding observational data~~ ~~simulated and corresponding OBS~~ are available,  
605 accounting for around ~~40~~50 % of the ~~model sample whole simulation~~ data. In each panel, the flux varies within the same  
interval range, between  $-50$  and  $400 \text{ Wm}^{-2}$  for  $H$  and  $LE$ , and between  $-50$  and  $500 \text{ Wm}^{-2}$  for  $H + LE$ . Moreover, the  
correlation coefficient is ~~around greater or equal to 0.9~~ ~~or greater~~, indicating that the variability in ~~MLP-based fluxes with data~~  
~~from the RegIPSL model~~  $MLP_{Grd1}$  fluxes is consistent with ~~actual observations (EC measurements or MLP-based estimates)~~.  
~~Hence, the differences between the fluxes mostly lie in their magnitudes~~  $OBS$  and  $MLP_{OBS}$ . These findings also hold for the  
610 second grid cell (Figure A3). ~~Hence, the disparities between simulated and observed fluxes mostly lie in their magnitudes.~~  
Since the difference is much more pronounced for large fluxes, the divergence would occur mainly during daylight hours. The  
~~MLP-based~~  $MLP_{Grd1}$   $H$  and  $H + LE$  ~~associated with the simulated environment~~ are stronger than observed. ~~It conforms to~~  
~~the tendency~~ ~~The same tendency has been~~ found when comparing simulated  $R_{net}$  to ~~observed observation~~ (not shown).

615

Figure 12 compares ~~3-hourly simulated turbulent~~ ~~hour simulated~~ heat fluxes at GrdPtGrd1 ~~to observations (left panels)~~  
~~and statistical estimates under simulated environment (right panels)~~ ( $SIM_{Grd1}$ ) to  $OBS$  and  $MLP_{Grd1}$  (left and right panels,  
~~respectively~~) at the same timestamps as in Figure 11. The scatter is considerably reduced with a better alignment along the  
linear regression fit when the ~~MLP-based fluxes are instead~~  $MLP_{Grd1}$  are used as the reference values ~~instead of OBS~~. These  
620 changes ~~are in agreement~~ ~~agree well~~ with a reduction of uncertainties, particularly those related to the ~~difference~~ ~~disparities~~  
in environmental conditions. ~~There is no ideal fit between simulated  $H + LE$  and corresponding~~ ~~The non-closure of SEB for~~  
MLP-based ~~estimates fluxes may~~ (Figure 12f) ~~because the statistical model does not allow SEB closure (Figure 7) and an~~  
~~important part of  $R_{net}$  is converted to soil heat flux throughout the simulation (not shown). This indicates that some substantial~~  
~~external~~ ~~7) explain the imperfect fit between  $SIM_{Grd1}$   $H + LE$  and corresponding  $MLP_{Grd1}$ . This suggests that substantial~~  
625 uncertainties remain. Nonetheless, comparing with ~~MLP-based estimates~~  $MLP_{Grd1}$  ~~better~~ highlights the shortcomings of the

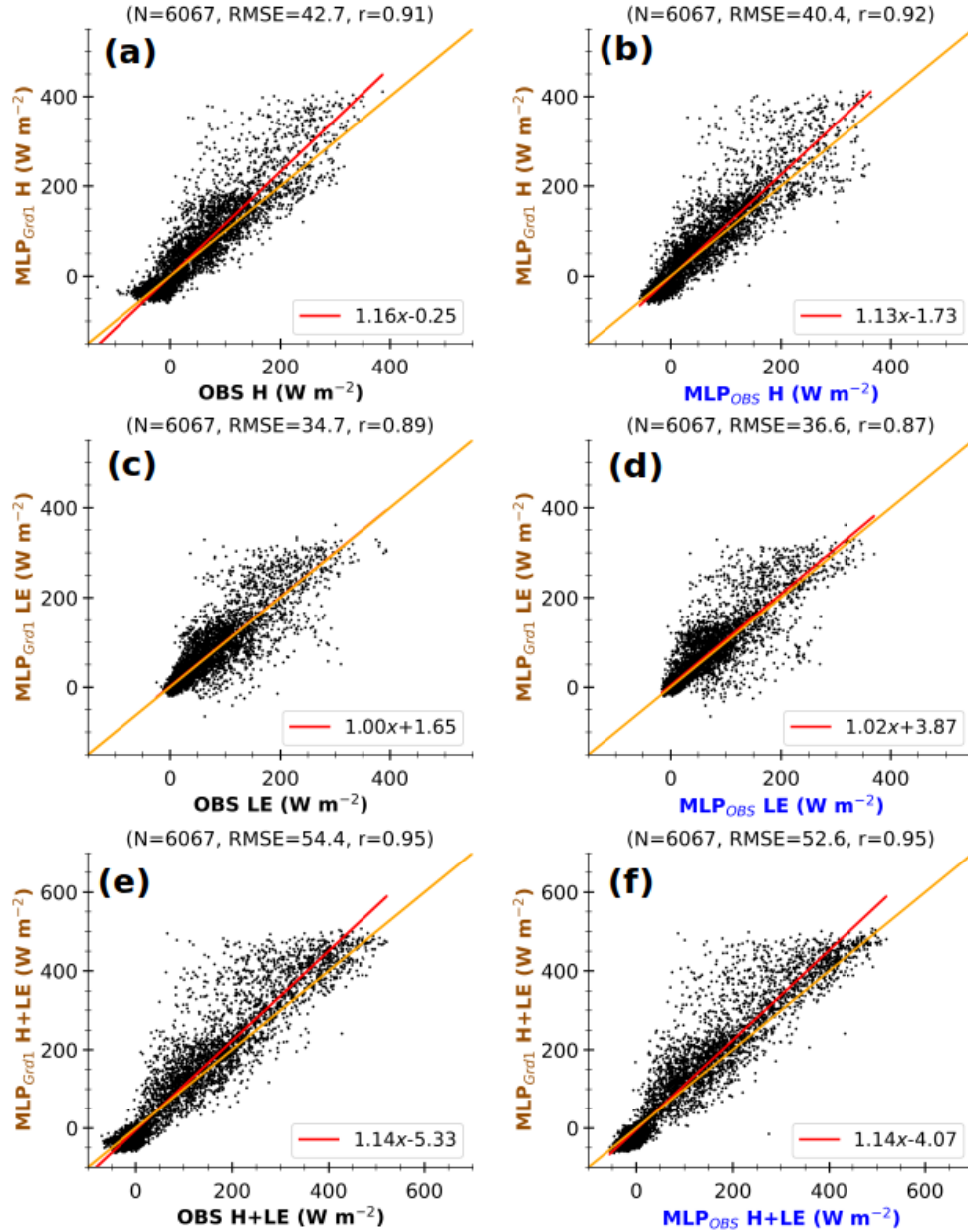


**Figure 11.** Comparison of 3-hourly-hour MLP-based fluxes in the simulated environment at GrdPtGrd1 (MLP<sub>Grd1</sub>) against 3-hour observations (a)OBS, e-and-eleft panels) and MLP-based fluxes in the observed-associated environment (MLP<sub>OBS</sub>, right panels) at Météopole site, for H (a, b), LE (c, d) and H + LE (e, f)at Météopole. It The data includes only considers model-3-hourly-hour timestamps between 24 November 2012 and 31 December 2016, for which both simulation and observational data are available. The values at the top of each panel correspond to the number of samples ( $N$ ), Root-Mean-Square-Error ( $RMSE$ ) and Pearson's correlation coefficient ( $r$ ). The lines in magenta-red and orange represent the linear regression and identical fits, respectively. The axis labels are coloured according to the schematic illustration in Figure 1.

surface scheme ~~better than comparing with observed data~~ than a direct comparison with *OBS*, as the bias in  $R_{net}$  is frozen. According to the ~~MLP-based fluxes in the simulated environment~~  $MLP_{Grd1}$ , the surface scheme tends to quasi-systematically underestimate large  $H$  (Figure 12a and b). This tendency is more pronounced for ~~the second grid cell~~  $Grd2$  (Figure A4), which comprises a ~~greater fraction of crops~~ smaller fraction of bare soil and a larger cropland fraction, which enhances evaporation.

630 Whereas, the simulated environment promotes overestimating large observed  $H$  (~~Figure 11~~ Figures 11 and A3, a and b), mostly due to higher  $R_{net}$  and weaker  $SM$ . Thus, ~~the bias in simulated fluxes~~ by using the statistical model, we can detect that the  $R_{net}$  overestimation compensates and hides an underestimation of  $H$  in RegIPSL. This underestimation can be due may be due to i) incorrect surface ~~heterogeneities~~ land use (with crop instead of grass and bare soil instead of urban area) ~~together with~~ and ii) inadequate formulations of fluxes.

635 Furthermore, ~~the simulated fluxes at the two grid cells~~ Additionally,  $SIM_{Grd1}$  and  $SIM_{Grd2}$  differ very slightly. As a result, the direct comparison with observations leads to nearly similar RMSE and correlation. Meanwhile, ~~the use of using~~ MLP-based estimates shows better performance at  $GrdPt1$ , since the landscape at  $GrdPt2$  induces fluxes shows a larger departure for  $Grd2$ , since its landscape induces slightly drier soil on average (Figure A1i). Thus, ~~it appears that the formulations of~~  $H$  and  $LE$  formulations in ORCHIDEE ~~in ORCHIDEE appear to~~ lack sensitivity to soil wetness.

640

Another key advantage of our method is that ~~all the data on any~~ simulation timestamps can be used ~~for comparison~~, since the availability of ~~observations at~~ the same timestamps ~~in the observations~~ is no longer ~~needed~~ necessary. The statistical significance of the ~~comparison results~~ is thus enhanced. Overall, including all the timestamps between 01 January 2012 and 31 December 2016 in the comparison does not change a lot the previous finding that the surface scheme struggles with large

645  $H$  (Figure A5).

~~In Figure 13, the comparison of~~ The seasonal cycles of  $SIM_{Grd1}$  and  $SIM_{Grd2}$ ,  $OBS$ ,  $MPL_{OBS}$  and  $MPL-MPL_{Grd1}$  and  $MPL_{Grd2}$  for  $H$ ,  $LE$  and  $H + LE$  ~~between simulation (magenta), observations (black), MLP-based estimates in the observed environment (cyan) and MLP-based estimates in simulated environment (orange)~~ shows that: ~~in Figure 13 show the following:~~

650 – The total flux  $H + LE$  is strongly affected by the environmental conditions, and the Simulated fluxes during the spring and summer seasons (from April to August) are the most tricky to evaluate because of significant differences in environmental forcing between simulation and observations. The direct comparison between simulation and observations is mainly hampered by the systematic bias in simulated  $R_{net}$  (Figure A6). This overestimation of  $R_{net}$  is no doubt



due to more short-wave radiation reaching the surface caused by a lack of low clouds in numerical simulation, as found in several modelling studies over mid-latitude (e.g. Cheruy et al., 2014; Bastin et al., 2018; Chakroun et al., 2018). Moreover, comparing  $SIM_{Grd}$  fluxes against  $MLP_{Grd}$  seems to mitigate the effect of the SEB non-closure problem does not seem to influence a lot the results of comparison with both observations and MLP-based estimates in observations. Indeed, the data-driven model captures the non-closure of SEB in the observations tends to underestimate strong values of  $RES$  (section 4, Figure 2). Hence, if this effect was so strong the MLP-based  $MLP_{Grd} H + LE$  in the simulated environment would have been much weaker than the simulated  $SIM_{Grd} H + LE$ , which is not necessarily the case. Thus, the differences between observations and simulations mainly rely on the overestimation of  $R_{net}$  in the simulation during the spring and summer months (From April to August, Figure A6). This overestimation of  $R_{net}$  is likely due to more shortwave radiation reaching the surface because of a lack of clouds, as already mentioned by several modelling studies over mid-latitude (e.g. Cheruy et al., 2014; Bastin et al., 2018; Chakroun et al., 2018). (Figure 13).

- Strikingly, the partitioning between  $H$  and  $LE$  in June, July, and August differs between simulated fluxes and MLP-based estimates in the simulated environment. The effective fraction occupied by the crops  $SIM_{Grd}$  and  $MLP_{Grd}$ . The fraction of grid cell effectively occupied by vegetation (crops and grass) is at its maximum during the summer months (not shown). The. Hence, the larger  $R_{net}$  in the simulation mainly leads to higher simulated  $LE$  than observed. Whereas, this stronger energy is converted into higher  $H$  and weaker  $LE$  by the statistical model, especially at the grid cell with the smaller fraction of bare soil to mimic what it has learned from observations. This is somewhat consistent with the fact that urban surfaces are not represented in ORCHIDEE and are replaced by bare soil, which evaporates more than impervious surfaces.
- As mentioned above, the simulated heat fluxes are not very well sensitive to soil wetness, whilst the MLP-based estimates are. Hence, the two grid cells show important differences for the MLP-based fluxes while not for the simulated fluxes. The variable  $SM$  is weaker at GridPt1 On average, the soil at Grid2 than at GridPt1 is drier between May and September (not shown Figure A7), which explains higher MLP-based the relatively higher  $MLP_{Grd2} H$  and lower MLP-based  $MLP_{Grd2} LE$  during this period, compared with  $MLP_{Grd1}$  fluxes. The same results are found when all the diurnal cycles of the model sample data are considered (Figure A8). This deficiency opens an avenue for improvements in ORCHIDEE.

There is clear evidence that the simulated  $H$  and  $LE$  are highly biased from late spring to late summer. This is undoubtedly due to an inappropriate representation of ~~the land cover together with~~ land cover and inaccurate weather conditions. Our statistical model also shows low generalization ability ~~over~~ during this period (Figure 8), illustrating the challenge of using environmental variables to parameterize surface turbulent heat fluxes that include contributions from heterogeneous patches. ~~Nonetheless, the~~  
685 ~~use of this~~ However, using the statistical model shows ~~very~~ consistent differences between the two grid cells ~~that are not so~~  
~~, which are not as~~ evident when using observations. ~~Indeed, the~~ The MLPs were trained on observed fluxes involving ~~urban~~  
~~contribution, and urban surfaces~~ contribution from urban land use types, whereas urban areas were replaced by bare soil in  
the version of ORCHIDEE used in the RegIPSL model. Yet, ~~the bare soil evaporates much more and heats~~ bare soil heats the  
atmosphere less than impervious surfaces such as urban areas. ~~As expected, the errors are lower at the grid cell with a greater~~  
690 ~~fraction of bare soil. According to the MLP-based fluxes, the environmental forcing discrepancies between observations and~~  
~~simulations appear to be the main source of uncertainty for a direct comparison at the seasonal scale, compared to the recurrent~~  
~~SEB imbalance in observations. Within the simulated environment, This likely explains why~~ the surface scheme ~~in the RegIPSL~~  
~~model~~ tends to underestimate large  $H$  and ~~then inversely,~~ conversely, overestimate the associated  $LE$  ~~. This certainly when~~  
evaluated in the simulated environment using the data-driven model. Since bare soil typically evaporates less than vegetated  
695 areas, the errors are relatively smaller for the nearest grid cell, likely due to its higher proportion of bare soil. This limitation  
in the land surface scheme likely contributes to a ~~poor representation of~~ misrepresentation of the intense convective heating of  
the ~~lower atmosphere during the late summer when heating predominates over evaporation.~~ atmosphere by the surface during  
the summer. Efforts are ongoing to improve the representation of urban areas in ORCHIDEE (e.g., Lalonde et al., 2024).

## 6 Conclusions

700 The representation of ~~the near-surface~~ surface processes, especially the formulation of surface turbulent heat fluxes  $H$  and  
 $LE$  is the second most important source of ~~error~~ biases in the numerical weather and climate simulations. However, it is  
very challenging to unambiguously quantify this error with the existing evaluation methods. In the framework of the MOSAI  
project (Lohou et al., 2022), this study proposes a different evaluation approach when a long period of comprehensive  
observational data is available. Based on the ~~observed cases~~ observations, a data-driven statistical model is first developed to  
705 approximate observed  $H$  and  $LE$  with near-surface environmental factors as inputs. The data-driven model is then applied  
to the simulated environment to generate ~~potentially~~ possibly observed fluxes under this environment. By comparing the  
simulated fluxes against ~~the~~ their statistically-based estimates, the evaluation is performed in the environment as seen by the

numerical model.

710 A demonstration study was carried out with about 10 consecutive years of observational data acquired at one of the permanent French instrumented sites of the ~~ACTRIS~~-ACTRIS-FR research network. The data-driven ~~statistical~~ model is a collection of several multi-layer perceptrons, trained on the data of the 5 most covered years after cleaning. Thirteen variables characterizing the environmental forcing in the surface layer are used as inputs to simultaneously provide estimates of observed  $H$  and  $LE$ . The analysis of variables contribution showed that the estimates are largely based on three classical physical parameters, 715 namely the surface net radiative flux, the mean potential temperature of the surface layer and the wetness of underlying soil. This opens the possibility to reduce the number of input parameters. Overall, the ~~estimated~~-statistically-based fluxes under observed conditions are rather consistent with the observed fluxes for known and unknown cases by the MLPs. Similar to the observed fluxes, the estimated fluxes do not close the Surface-Energy-Budget. ~~Thus, this data-driven model can be convenient for gap-filling, especially under wet conditions, but reduce its impact.~~ Nevertheless, it does not correctly approximate negative 720  $H$  and tends to underestimate large  $LE$ . Moreover, its ability to generalize is altered from spring to late summer, likely because the leading input parameters do not fully describe the strong inter-annual variability in this period. This limitation can probably be overcome by adding a typical vegetation parameter (e.g.  $LAI$ ) to the inputs.

The data-driven model was subsequently applied to a regional climate simulation performed with the RegIPSL model to 725 freeze the uncertainties which may come from the inaccuracy of simulated environmental forcing. The simulation data were extracted at the two nearest grid cells to the station. The comparison between simulated and observed fluxes gives the error resulting from the compensation between the components of the numerical model. The noticeable difference is found from late spring to late summer, in agreement with the previous studies. Overall, both simulated  $H$  and  $LE$  are stronger than observed, in consistency with stronger net radiative flux. The comparison of simulated and statistically-based heat fluxes in the 730 simulated environment revealed that the ~~incorrect~~-numerical formulation of fluxes combined with the inconsistency of surface characteristics in the grid cells mainly cause an underestimation of large  $H$  and an overestimation of associated  $LE$ , which were hidden by the overestimation of  $R_{net}$ . Moreover, the partitioning between heating and evaporation is not ~~very properly~~ sensitive to soil moisture.

735 By circumventing the challenge of comparing the turbulent heat fluxes from different environments, our evaluation method offers promising perspectives for adequate evaluation of the surface parametrization schemes. The ~~ACTRIS-France~~-ACTRIS-FR

network offers the possibility of applying this methodology to other supersites where the variables required for this analysis have been also measured for several years, allowing investigation in different types of surfaces and climates. The ReOBS approach (Chiriaco et al., 2018) has been applied to these long-term colocated multi-variables datasets, which eases their use  
740 for different applications.

At this early stage, our proposed approach firstly focused on discrepancies in environmental forcing between simulation and observation. However, the non-closure of SEB and the representativeness of in-situ measurements at the horizontal resolution of the numerical models are also key sources of uncertainties. Hence, our evaluation method should be further refined to  
745 address these two challenges, ensuring a better agreement with the simplifying assumptions used in the numerical models.  
Thanks to the MOSAI project, ~~each of these sites has the~~ Toulouse region benefited from a one-year enhanced ~~observing period for a better~~ observation period, which would allow a more detailed regional-scale characterization of the ~~representativity of the long-term fluxes stations, which is crucial information for model evaluation. Moreover, the statistical model could be developed under the fundamental assumption of SEB closure (e.g., Hu et al., 2021) used in the numerical weather and climate~~  
750 representativeness of the fluxes measured at the Météopole permanent station (Jomé et al., 2023). For instance, the input variables for the data-driven model could incorporate a description of land use composition. In addition, this model may learn to estimate observed fluxes that verify the closure of SEB (e.g., Hu et al., 2021), usually applied in numerical models.  
There is also a need to include a transfer learning strategy to prevent the possible ~~loss~~ deterioration of performance when the ~~statistical data-driven~~ model is applied to ~~eases~~ situations with the leading input ~~parameters~~ variables ranging out of its known  
755 domain. Besides, this novel approach could be used to evaluate community numerical simulations like reanalysis and to revisit ~~the~~ intercomparison of land-surface schemes.

*Data availability.* The data from the Météopole are freely available on AERIS platform (<https://www.aeris-data.fr/>). The source for RegIPSL data is indicated in the acknowledgements.

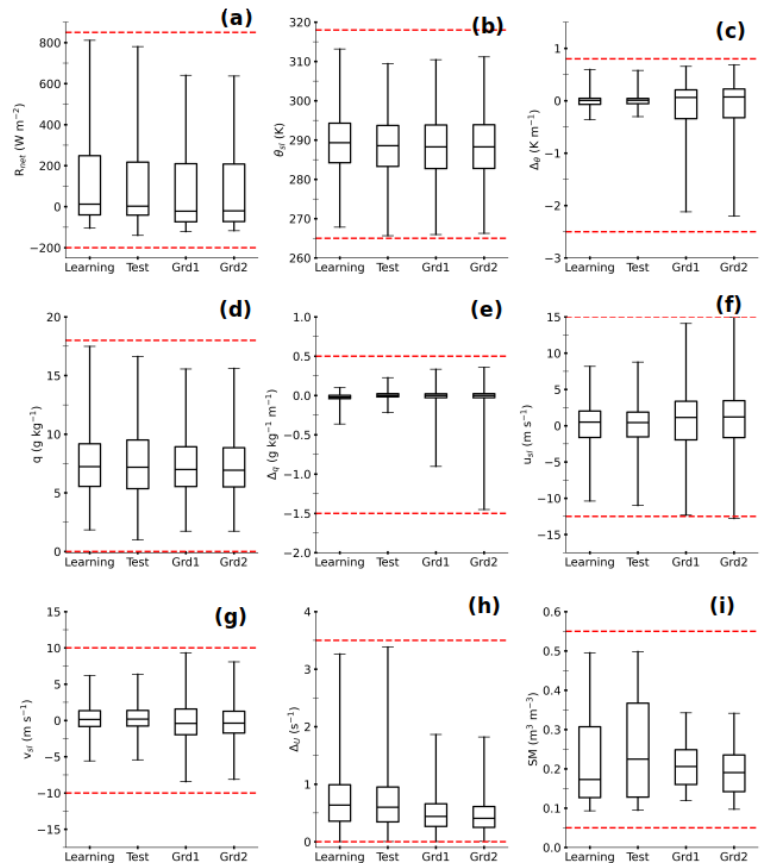


**Figure A1.** Box plots summarizing the interval ranges of the nine physical variables used as input to our MLP-based statistic model (Table 2). The corresponding data sets are indicated on the  $x$ -axis. The whiskers represent the minimum and maximum values of each data set. The horizontal dashed red lines indicate the extreme values used for scaling.

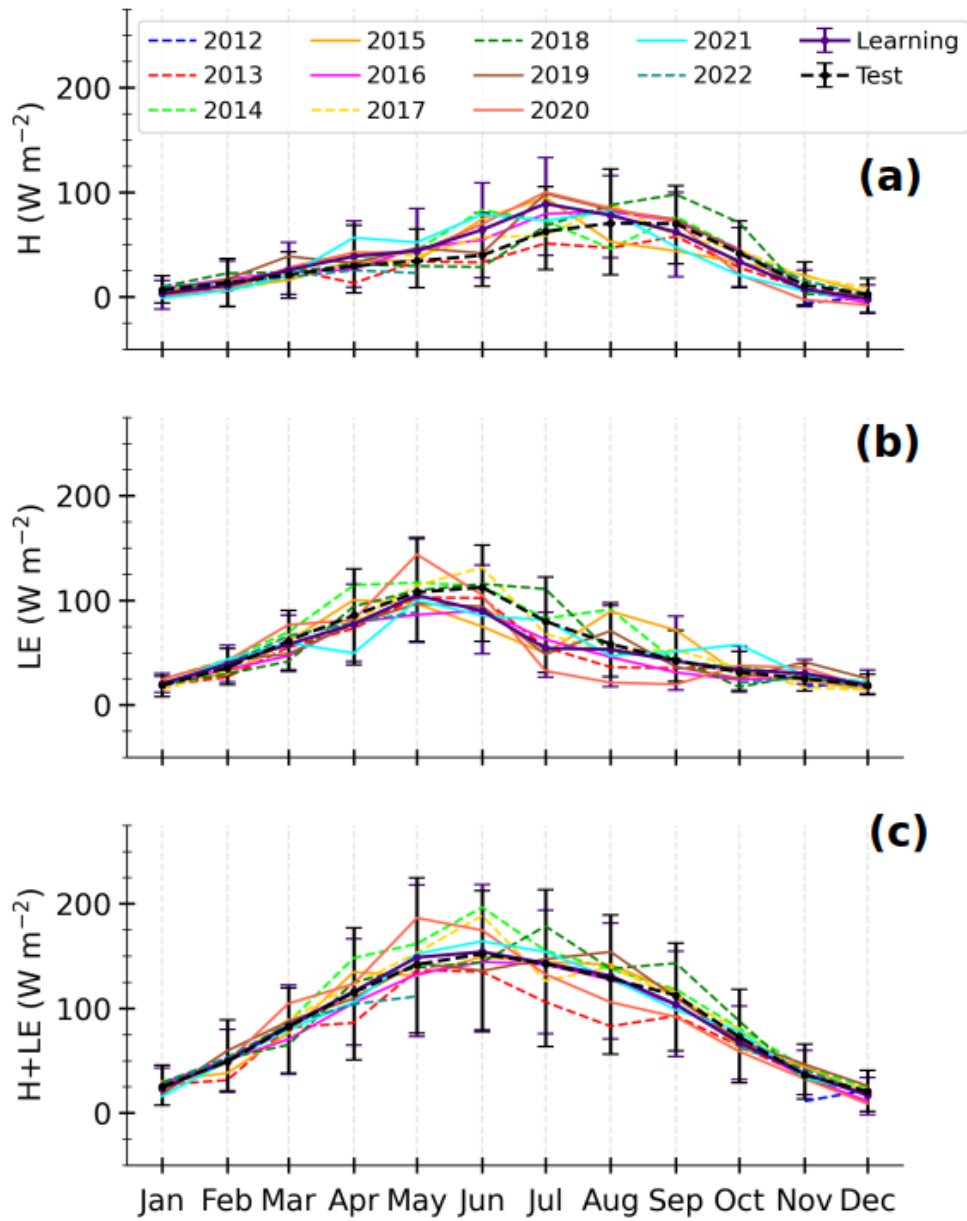


**Figure A2.** Composite monthly averages of observed sensible heat flux ( $H$ , a), latent heat flux ( $LE$ , b) and total turbulent heat flux ( $H + LE$ , c) for each year included in the observational data, calculated from the daily averages of half-hourly samples. The years of learning and test sets are in solid and dashed lines, respectively. The thick lines correspond to the means on each subset, and the error represents the 10 and 90<sup>th</sup> percentiles.

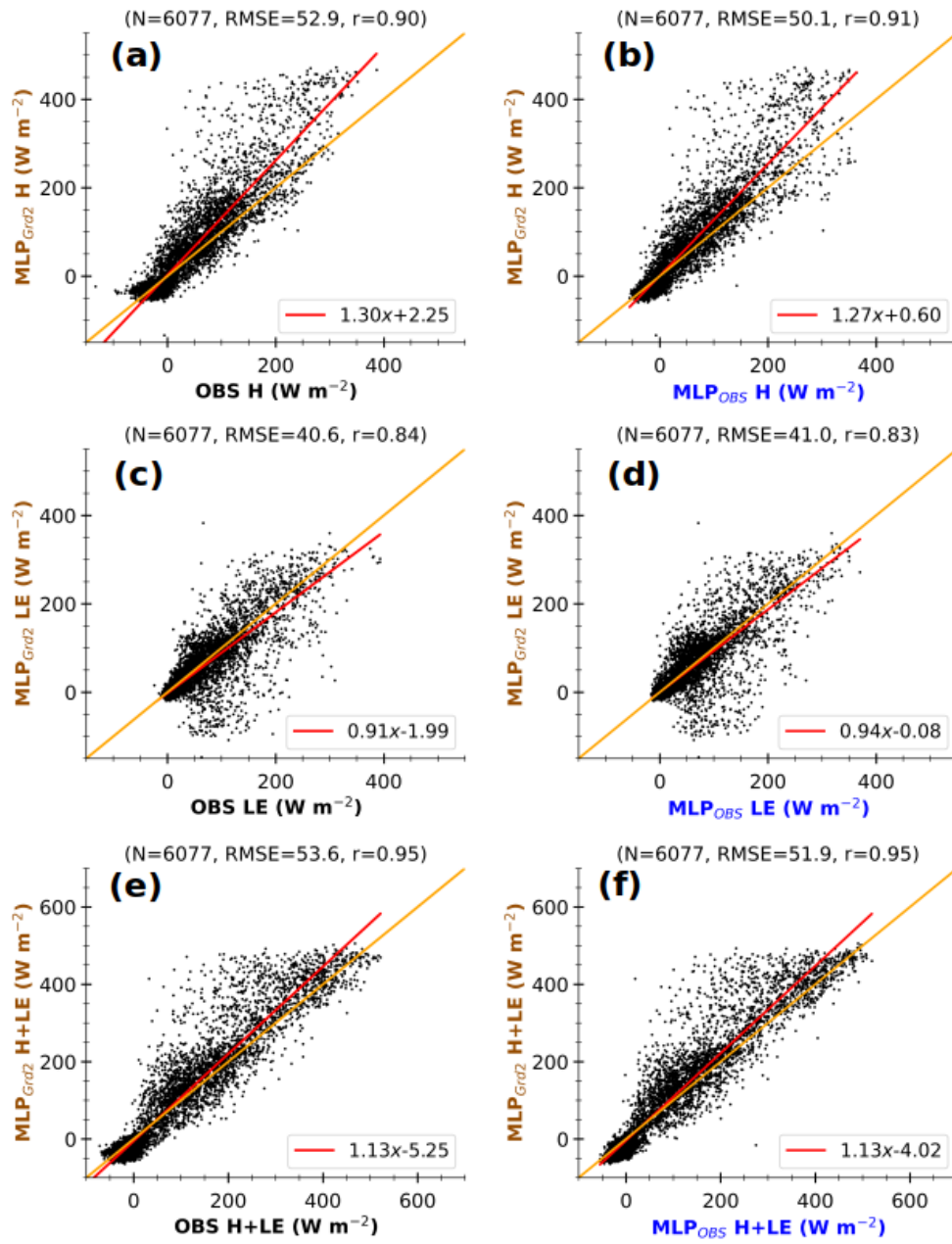
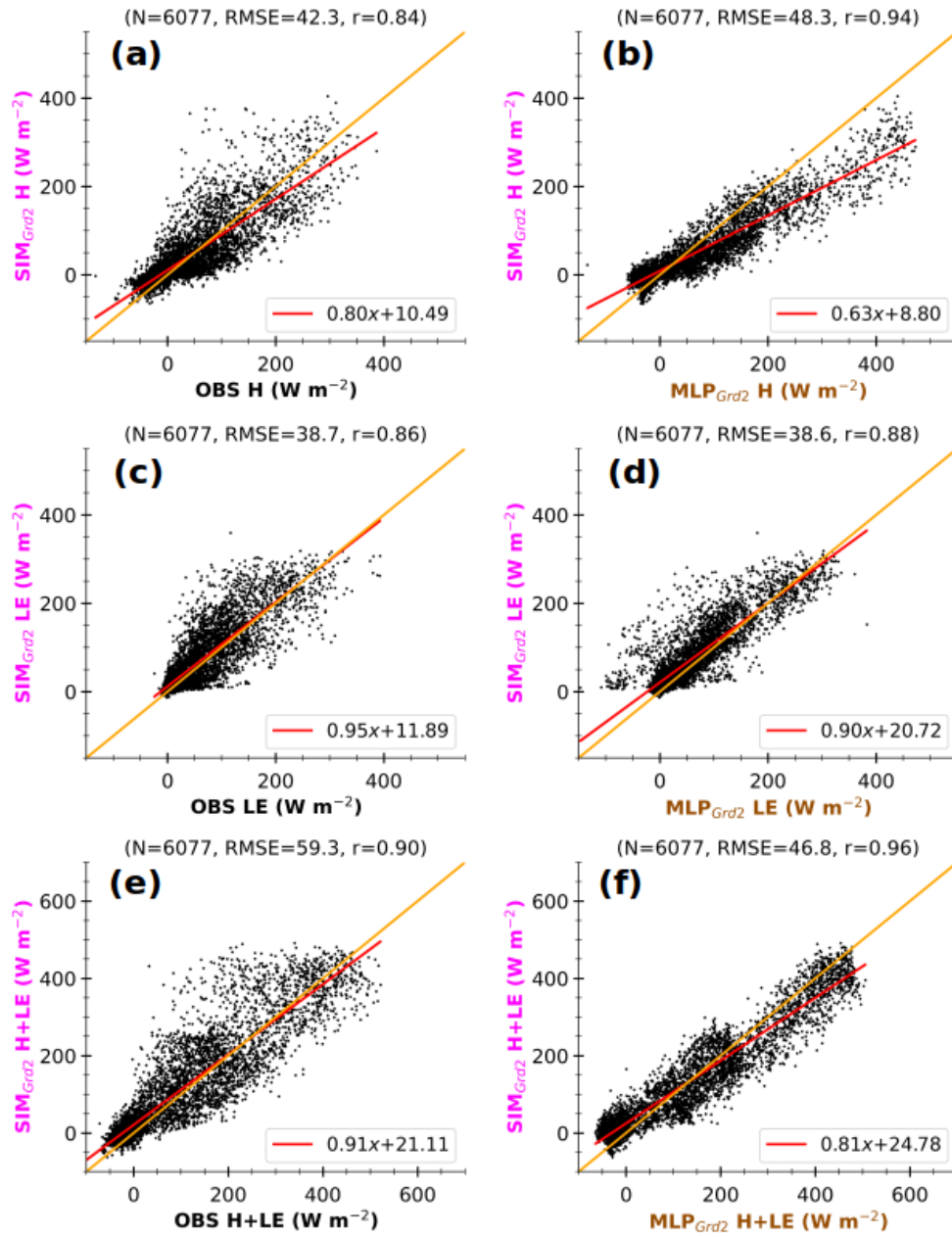
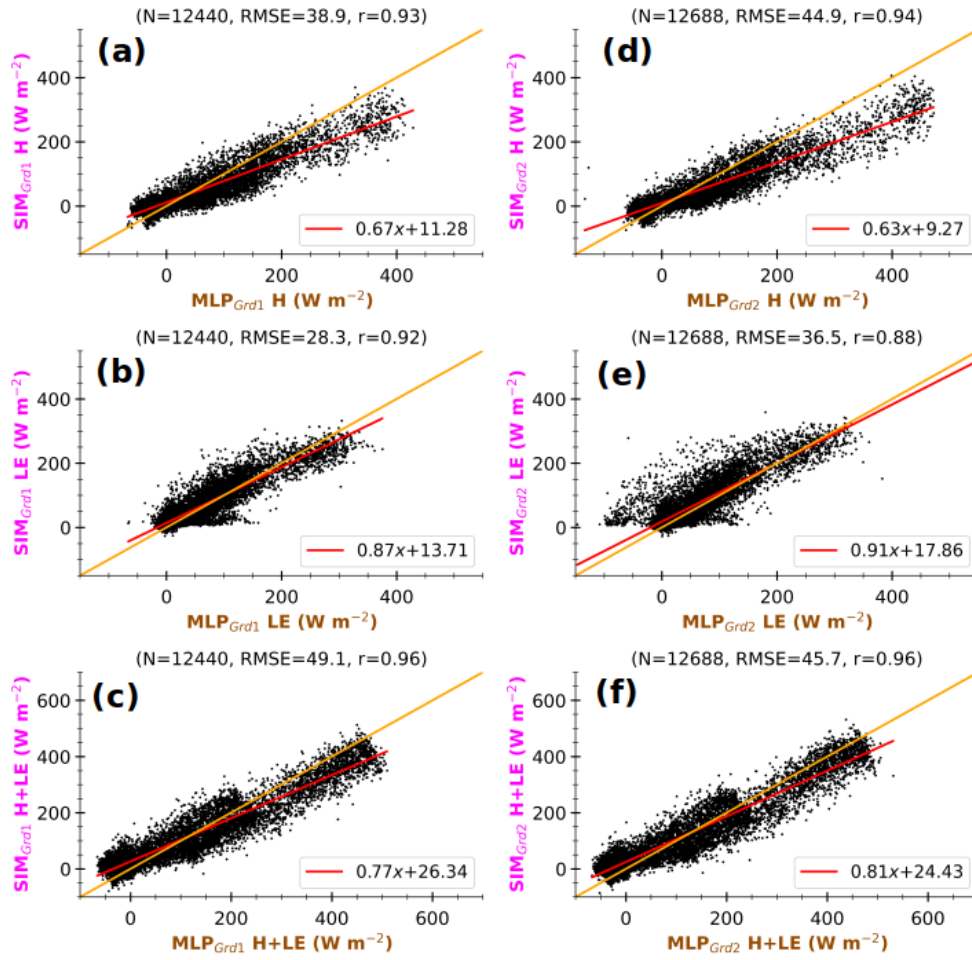


Figure A3. Same as in Figure 11 but for GrdPtGrd2.



**Figure A4.** Same as in Figure 12 but for GrdPtGrd2.





**Figure A5.** 3-hourly simulated sensible heat flux ( $H$ , a and d), latent heat flux ( $LE$ , b and e) and total turbulent heat flux ( $H + LE$ , c and f) at GrdPtGrd1 (left panels) and GrdPtGrd2 (right panels) against corresponding MLP-based estimates in simulated environment. All the selected timestamps from 01 January 2012 to 31 December 2016 are considered here. The values at the top of each panel correspond to the number of samples ( $N$ ), Root-Mean-Square-Error ( $RMSE$ ) and Pearson's correlation coefficient ( $r$ ). The lines in magenta-red and orange represent the linear and ideal fits, respectively. The axis labels are colored according to the schematic illustration in Figure 1.

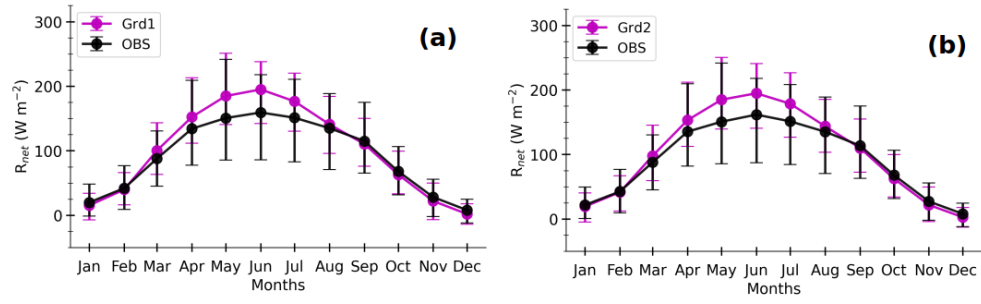


**Figure A6.** Composites monthly averages of simulated surface net radiative flux ( $R_{net}$ , magenta lines) at GrdPtGrd1 (a) and GrdPt2-Grd2 (b) and that of their respective observations at Météopole (black lines). They are computed as in Figure 13.

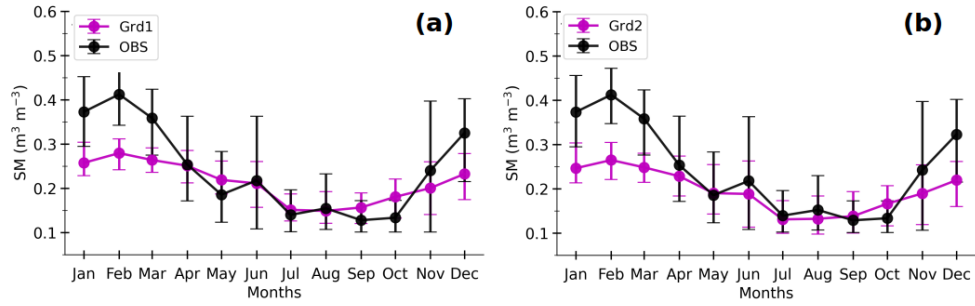


**Figure A7.** Same as in Figure A6 but for soil wetness (SM).

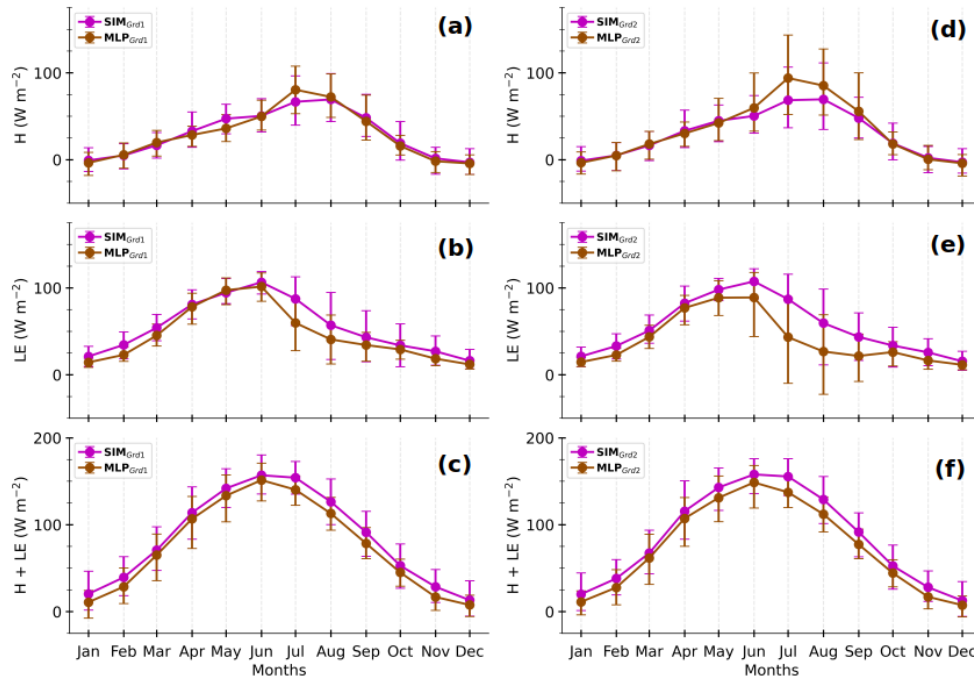


**Figure A8.** Composites monthly averages of simulated sensible heat flux ( $H$  ; (a and d), latent heat flux ( $LE$  ; (b and e) and total turbulent heat flux ( $H + LE$  ; (c and f) at GrdPtGrd1 and GrdPtGrd2 (magenta  $SIM_{Grd1}$  and  $SIM_{Grd2}$  lines in left and right panels resp. magenta) together with that of MLP-based estimates under simulated environment (orange  $MLP_{Grd1}$  and  $MLP_{Grd2}$  lines resp. in brown). The solid lines correspond to the means and the error bars represent the 10 and 90<sup>th</sup> percentiles, calculated by gathering the daily averages of 3-hourly data. All the selected diurnal cycles from 01 January 2012 to 31 December 2016 are considered here.

*Author contributions.* MZ, SB and MC elaborated the methodology with contributions from CM and LB. GC and SB provided the observational and climate simulation data respectively. MZ processed the data and prepared the paper with contributions from all the co-authors.

*Competing interests.* The authors declare that they have no conflict of interest.

*Acknowledgements.* The MOSAI (Model and Observation for Surface-Atmosphere Interactions) project was founded by the French Agence Nationale de la Recherche (ANR) under grant agreement no. 216875. The RegIPSL simulation was granted access to the HPC resources

of IDRIS under the allocation 2019-0227 attributed by GENCI (Grand ~~Equipement~~ Équipement National de Calcul Intensif). Thanks to  
775 ESPRI-IPSL and LATMOS IT department for access to the computational and storage infrastructures.

## References

- Abadi, M., Barham, P., Chen, J., Chen, Z., Davis, A., Dean, J., Devin, M., Ghemawat, S., Irving, G., Isard, M., Kudlur, M., Levenberg, J., Monga, R., Moore, S., Murray, D. G., Steiner, B., Tucker, P., Vasudevan, V., Warden, P., Wicke, M., Yu, Y., and Zheng, X.: TensorFlow: A System for Large-Scale Machine Learning, <https://doi.org/10.48550/arXiv.1605.08695>, comment: 18 pages, 9 figures; v2 has a spelling correction in the metadata, 2016.
- Abramowitz, G.: Towards a Benchmark for Land Surface Models, *Geophysical Research Letters*, 32, <https://doi.org/10.1029/2005GL024419>, 2005.
- Aggarwal, C. C.: Rare Class Learning, in: *Data Classification*, Chapman and Hall/CRC, ISBN 978-0-429-10263-9, 2014.
- Alléon, J.: Description of the Energy Budgets in ORCHIDEE, Technical Report, Laboratoire des Sciences du Climat et de l'Environnement, Paris, France, 2022.
- Andersen, T. and Martinez, T.: Cross Validation and MLP Architecture Selection, in: *IJCNN'99. International Joint Conference on Neural Networks. Proceedings (Cat. No.99CH36339)*, vol. 3, pp. 1614–1619, IEEE, Washington, DC, USA, ISBN 978-0-7803-5529-3, <https://doi.org/10.1109/IJCNN.1999.832613>, 1999.
- Arjdal, K., Vignon, É., Driouech, F., Chérut, F., Er-Raki, S., Sima, A., Chehbouni, A., and Drobinski, P.: Modeling Land–Atmosphere Interactions over Semiarid Plains in Morocco: In-Depth Assessment of GCM Stretched-Grid Simulations Using In Situ Data, *Journal of Applied Meteorology and Climatology*, 63, 369–386, <https://doi.org/10.1175/JAMC-D-23-0099.1>, 2024.
- Aubinet, M., Vesala, T., and Papale, D., eds.: *Eddy Covariance: A Practical Guide to Measurement and Data Analysis*, Springer Netherlands, Dordrecht, ISBN 978-94-007-2350-4 978-94-007-2351-1, <https://doi.org/10.1007/978-94-007-2351-1>, 2012.
- Bastin, S., Chiriaco, M., and Drobinski, P.: Control of Radiation and Evaporation on Temperature Variability in a WRF Regional Climate Simulation: Comparison with Colocated Long Term Ground Based Observations near Paris, *Clim Dyn*, 51, 985–1003, <https://doi.org/10.1007/s00382-016-2974-1>, 2018.
- Bonavita, M. and Laloyaux, P.: Machine Learning for Model Error Inference and Correction, *J Adv Model Earth Syst*, 12, <https://doi.org/10.1029/2020MS002232>, 2020.
- Bonnasse-Gahot, L.: Interpolation, Extrapolation, and Local Generalization in Common Neural Networks, <https://doi.org/10.48550/arXiv.2207.08648>, 2022.
- Breiman, L.: Bagging Predictors, *Mach Learn*, 24, 123–140, <https://doi.org/10.1007/BF00058655>, 1996.
- Chakroun, M., Bastin, S., Chiriaco, M., and Chepfer, H.: Characterization of Vertical Cloud Variability over Europe Using Spatial Lidar Observations and Regional Simulation, *Clim Dyn*, 51, 813–835, <https://doi.org/10.1007/s00382-016-3037-3>, 2018.
- Cherut, F., Dufresne, J. L., Hourdin, F., and Ducharne, A.: Role of Clouds and Land-Atmosphere Coupling in Midlatitude Continental Summer Warm Biases and Climate Change Amplification in CMIP5 Simulations, *Geophysical Research Letters*, 41, 6493–6500, <https://doi.org/10.1002/2014GL061145>, 2014.

- Chicco, D.: Ten Quick Tips for Machine Learning in Computational Biology, *BioData Mining*, 10, 35, <https://doi.org/10.1186/s13040-017-0155-3>, 2017.
- Chiriaco, M., Dupont, J.-C., Bastin, S., Badosa, J., Lopez, J., Haeffelin, M., Chepfer, H., and Guzman, R.: ReOBS: A New Approach to Synthesize Long-Term Multi-Variable Dataset and Application to the SIRTAS Supersite, *Earth Syst. Sci. Data*, 10, 919–940, <https://doi.org/10.5194/essd-10-919-2018>, 2018.
- Coppola, E., Sobolowski, S., Pichelli, E., Raffaele, F., Ahrens, B., Anders, I., Ban, N., Bastin, S., Belda, M., Belusic, D., Caldas-Alvarez, A., Cardoso, R. M., Davolio, S., Dobler, A., Fernandez, J., Fita, L., Fumiere, Q., Giorgi, F., Goergen, K., Güttler, I., Halenka, T., Heinzeller, D., Hodnebrog, Ø., Jacob, D., Kartsios, S., Katragkou, E., Kendon, E., Khodayar, S., Kunstmann, H., Knist, S., Lavín-Gullón, A., Lind, P., Lorenz, T., Maraun, D., Marelle, L., van Meijgaard, E., Milovac, J., Myhre, G., Panitz, H.-J., Piazza, M., Raffa, M., Raub, T., Rockel, B., Schär, C., Sieck, K., Soares, P. M. M., Somot, S., Srncic, L., Stocchi, P., Tölle, M. H., Truhetz, H., Vautard, R., de Vries, H., and Warrach-Sagi, K.: A First-of-Its-Kind Multi-Model Convection Permitting Ensemble for Investigating Convective Phenomena over Europe and the Mediterranean, *Clim Dyn*, 55, 3–34, <https://doi.org/10.1007/s00382-018-4521-8>, 2020.
- Cybenko, G.: Approximation by Superpositions of a Sigmoidal Function, *Math. Control Signal Systems*, 2, 303–314, <https://doi.org/10.1007/BF02551274>, 1989.
- Daumé III, H.: Frustratingly Easy Domain Adaptation, <https://doi.org/10.48550/arXiv.0907.1815>, 2009.
- Day, O. and Khoshgoftaar, T. M.: A Survey on Heterogeneous Transfer Learning, *Journal of Big Data*, 4, 29, <https://doi.org/10.1186/s40537-017-0089-0>, 2017.
- de Burgh-Day, C. O. and Leeuwenburg, T.: Machine Learning for Numerical Weather and Climate Modelling: A Review, *Geoscientific Model Development*, 16, 6433–6477, <https://doi.org/10.5194/gmd-16-6433-2023>, 2023.
- de Mathelin, A., Atiq, M., Richard, G., de la Concha, A., Yachouti, M., Deheeger, F., Mougeot, M., and Vayatis, N.: ADAPT : Awesome Domain Adaptation Python Toolbox, comment: 11 pages, 6 figures, 2023.
- Ducharne, A., Ottlé, C., Maignan, F., Vuichard, N., Ghattas, J., Wang, F., Peylin, P., Polcher, J., Guimberteau, M., Maugis, P., Tafasca, S., Tootchi, A., Verhoef, A., and Mizuochi, H.: The Hydrol Module of ORCHIDEE: Scientific Documentation [Rev 3977] and on, Work in Progress, towards CMIP6v1, Technical Report, Institut Pierre Simon Laplace, Paris, France, 2018.
- Ducoudré, N. I., Laval, K., and Perrier, A.: SECHIBA, a New Set of Parameterizations of the Hydrologic Exchanges at the Land-Atmosphere Interface within the LMD Atmospheric General Circulation Model, *Journal of Climate*, 6, 248–273, [https://doi.org/10.1175/1520-0442\(1993\)006<0248:SANSOP>2.0.CO;2](https://doi.org/10.1175/1520-0442(1993)006<0248:SANSOP>2.0.CO;2), 1993.
- Etienne, J.: Meteorological, Soil Data and Surface Turbulent Fluxes - Meteopole Station., <https://doi.org/10.25326/44>, 2022.
- Fernando, B., Habrard, A., Sebban, M., and Tuytelaars, T.: Unsupervised Visual Domain Adaptation Using Subspace Alignment, in: 2013 IEEE International Conference on Computer Vision, pp. 2960–2967, IEEE, Sydney, Australia, ISBN 978-1-4799-2840-8, <https://doi.org/10.1109/ICCV.2013.368>, 2013.

- Foken, T., Aubinet, M., Finnigan, J. J., Leclerc, M. Y., Mauder, M., and U, K. T. P.: Results Of A Panel Discussion About The Energy Balance Closure Correction For Trace Gases, *Bulletin of the American Meteorological Society*, 92, ES13–ES18, <https://doi.org/10.1175/2011BAMS3130.1>, 2011.
- Frassoni, A., Reynolds, C., Wedi, N., Bouallègue, Z. B., Caltabiano, A. C. V., Casati, B., Christophersen, J. A., Coelho, C. A. S., Falco, C. D., Doyle, J. D., Fernandes, L. G., Forbes, R., Janiga, M. A., Klocke, D., Magnusson, L., McTaggart-Cowan, R., Pakdaman, M., Rushley, S. S., Verhoef, A., Yang, F., and Zängl, G.: Systematic Errors in Weather and Climate Models: Challenges and Opportunities in Complex Coupled Modeling Systems, *Bulletin of the American Meteorological Society*, 104, E1687–E1693, <https://doi.org/10.1175/BAMS-D-23-0102.1>, 2023.
- Ganaie, M. A., Hu, M., Malik, A. K., Tanveer, M., and Suganthan, P. N.: Ensemble Deep Learning: A Review, *Engineering Applications of Artificial Intelligence*, 115, 105 151, <https://doi.org/10.1016/j.engappai.2022.105151>, 2022.
- Gentine, P., Pritchard, M., Rasp, S., Reinaudi, G., and Yacalis, G.: Could Machine Learning Break the Convection Parameterization Dead-lock?, *Geophys. Res. Lett.*, 45, 5742–5751, <https://doi.org/10.1029/2018GL078202>, 2018.
- Goodfellow, I., Bengio, Y., and Courville, A.: *Deep Learning*, The MIT Press, Cambridge, Massachusetts, illustrated edition edn., ISBN 978-0-262-03561-3, 2016.
- Guion, A., Turquety, S., Polcher, J., Pennel, R., Bastin, S., and Arsouze, T.: Droughts and Heatwaves in the Western Mediterranean: Impact on Vegetation and Wildfires Using the Coupled WRF-ORCHIDEE Regional Model (RegIPSL), *Clim Dyn*, 58, 2881–2903, <https://doi.org/10.1007/s00382-021-05938-y>, 2022.
- Henderson-Sellers, A., McGuffie, K., and Pitman, A. J.: The Project for Intercomparison of Land-surface Parametrization Schemes (PILPS): 1992 to 1995, *Climate Dynamics*, 12, 849–859, <https://doi.org/10.1007/s003820050147>, 1996.
- Hornik, K., Stinchcombe, M., and White, H.: Multilayer Feedforward Networks Are Universal Approximators, *Neural Networks*, 2, 359–366, [https://doi.org/10.1016/0893-6080\(89\)90020-8](https://doi.org/10.1016/0893-6080(89)90020-8), 1989.
- Hu, X., Shi, L., and Lin, G.: The Data-Driven Solution of Energy Imbalance-Induced Structural Error in Evapotranspiration Models, *Journal of Hydrology*, 597, 126 205, <https://doi.org/10.1016/j.jhydrol.2021.126205>, 2021.
- Jomé, M., Lohou, F., Lothon, M., Canut, G., Couvreur, F., Brut, A., Derrien, S., Maurel, W., Etienne, J.-C., Vial, A., and Garrouste, O.: Evaluation of the Representativity of Reference Long-Term Surface Flux Measurements in an Heterogeneous Landscape : The M&eacute;T&eacute;Opole Campaign (MOSAI Project), *Tech. Rep. EMS2023-74*, Copernicus Meetings, <https://doi.org/10.5194/ems2023-74>, 2023.
- Kelley, J. and Pardyjak, E.: Using Neural Networks to Estimate Site-Specific Crop Evapotranspiration with Low-Cost Sensors, *Agronomy*, 9, 108, <https://doi.org/10.3390/agronomy9020108>, 2019.
- Kelley, J., McCauley, D., Alexander, G. A., Gray, W. F., Siegfried, R., and Oldroyd, H. J.: Using Machine Learning to Integrate On-Farm Sensors and Agro-Meteorology Networks into Site-Specific Decision Support, *Transactions of the ASABE*, 63, 1427–1439, <https://doi.org/10.13031/trans.13917>, 2020.

- 870 Khwaja, A. S., Naeem, M., Anpalagan, A., Venetsanopoulos, A., and Venkatesh, B.: Improved Short-Term Load Forecasting Using Bagged  
Neural Networks, *Electric Power Systems Research*, 125, 109–115, <https://doi.org/10.1016/j.epsr.2015.03.027>, 2015.
- Kingma, D. P. and Ba, J.: Adam: A Method for Stochastic Optimization, <https://doi.org/10.48550/arXiv.1412.6980>, comment: Published as  
a conference paper at the 3rd International Conference for Learning Representations, San Diego, 2015, 2017.
- Knutti, R., Stocker, T. F., Joos, F., and Plattner, G.-K.: Probabilistic Climate Change Projections Using Neural Networks, *Climate Dynamics*,  
875 21, 257–272, <https://doi.org/10.1007/s00382-003-0345-1>, 2003.
- Krinner, G., Viovy, N., de Noblet-Ducoudré, N., Ogée, J., Polcher, J., Friedlingstein, P., Ciais, P., Sitch, S., and Prentice, I. C.: A  
Dynamic Global Vegetation Model for Studies of the Coupled Atmosphere-Biosphere System, *Global Biogeochemical Cycles*, 19,  
<https://doi.org/10.1029/2003GB002199>, 2005.
- Kruse, R., Borgelt, C., Klawonn, F., Moewes, C., Steinbrecher, M., and Held, P.: Computational Intelligence: A Methodological Introduction,  
880 Texts in Computer Science, Springer, London, ISBN 978-1-4471-5012-1 978-1-4471-5013-8, <https://doi.org/10.1007/978-1-4471-5013-8>,  
2013.
- Kumar, M., Raghuwanshi, N. S., and Singh, R.: Artificial Neural Networks Approach in Evapotranspiration Modeling: A Review, *Irrig Sci*,  
29, 11–25, <https://doi.org/10.1007/s00271-010-0230-8>, 2011.
- Lalonde, M., Oudin, L., Ducharne, A., Bastin, S., and Arboleda-Obando, P.: Explicit Representation of Cities in the ORCHIDEE Land  
885 Surface Model, Tech. Rep. EGU24-6183, Copernicus Meetings, <https://doi.org/10.5194/egusphere-egu24-6183>, 2024.
- Leufen, L. H. and Schädler, G.: Calculating the Turbulent Fluxes in the Atmospheric Surface Layer with Neural Networks, *Geosci. Model  
Dev.*, 12, 2033–2047, <https://doi.org/10.5194/gmd-12-2033-2019>, 2019.
- Liu, G., Liu, Y., and Endo, S.: Evaluation of Surface Flux Parameterizations with Long-Term ARM Observations, *Monthly Weather Review*,  
141, 773–797, <https://doi.org/10.1175/MWR-D-12-00095.1>, 2013.
- 890 Lohou, F., Lothon, M., Bastin, S., Brut, A., Canut, G., Cheruy, F., Couvreur, F., Cohard, J.-M., Darrozes, J., Dupont, J.-C., Lafont, S.,  
Roehrig, R., and Román-Cascón, C.: Model and Observation for Surface Atmosphere Interactions (MOSAI) Project, Tech. Rep. EGU22-  
8797, Copernicus Meetings, <https://doi.org/10.5194/egusphere-egu22-8797>, 2022.
- Lundberg, S. and Lee, S.-I.: A Unified Approach to Interpreting Model Predictions, <https://doi.org/10.48550/arXiv.1705.07874>, comment:  
To appear in NIPS 2017, 2017.
- 895 Mauder, M. and Foken, T.: Documentation and Instruction Manual of the Eddy Covariance Software Package TK2, 2004.
- Mauder, M., Genzel, S., Fu, J., Kiese, R., Soltani, M., Steinbrecher, R., Zeeman, M., Banerjee, T., De Roo, F., and Kunstmann, H.: Evalu-  
ation of Energy Balance Closure Adjustment Methods by Independent Evapotranspiration Estimates from Lysimeters and Hydrological  
Simulations, *Hydrological Processes*, 32, 39–50, <https://doi.org/10.1002/hyp.11397>, 2018.
- Mauder, M., Foken, T., and Cuxart, J.: Surface-Energy-Balance Closure over Land: A Review, *Boundary-Layer Meteorol*, 177, 395–426,  
900 <https://doi.org/10.1007/s10546-020-00529-6>, 2020.
- Monin, A. and Obukhov, A.: Basic Laws of Turbulent Mixing in the Surface Layer of the Atmosphere, 1954.



- Pan, S. J., Tsang, I. W., Kwok, J. T., and Yang, Q.: Domain Adaptation via Transfer Component Analysis, *IEEE Transactions on Neural Networks*, 22, 199–210, <https://doi.org/10.1109/TNN.2010.2091281>, 2011.
- Polcher, J., McAvaney, B., Viterbo, P., Gaertner, M. A., Hahmann, A., Mahfouf, J. F., Noilhan, J., Phillips, T., Pitman, A., Schlosser, C. A.,  
 905 Schulz, J. P., Timbal, B., Verseghy, D., and Xue, Y.: A Proposal for a General Interface between Land Surface Schemes and General  
 Circulation Models, *Global and Planetary Change*, 19, 261–276, [https://doi.org/10.1016/S0921-8181\(98\)00052-6](https://doi.org/10.1016/S0921-8181(98)00052-6), 1998.
- Reddi, S. J., Kale, S., and Kumar, S.: ON THE CONVERGENCE OF ADAM AND BEYOND, 2018.
- Román-Cascón, C., Lothon, M., Lohou, F., Ojha, N., Merlin, O., Aragonés, D., González-Dugo, M. P., Andreu, A., Pellarin, T., Brut,  
 A., Soriguer, R. C., Díaz-Delgado, R., Hartogensis, O., and Yagüe, C.: Can We Use Satellite-Based Soil-Moisture Products at High  
 910 Resolution to Investigate Land-Use Differences and Land–Atmosphere Interactions? A Case Study in the Savanna, *Remote Sensing*, 12,  
 1701, <https://doi.org/10.3390/rs12111701>, 2020.
- Román-Cascón, C., Lothon, M., Lohou, F., Hartogensis, O., Vila-Guerau de Arellano, J., Pino, D., Yagüe, C., and Pardyjak, E. R.: Surface  
 Representation Impacts on Turbulent Heat Fluxes in the Weather Research and Forecasting (WRF) Model (v.4.1.3), *Geosci. Model Dev.*,  
 14, 3939–3967, <https://doi.org/10.5194/gmd-14-3939-2021>, 2021.
- 915 Rosenblatt, F.: Perceptron Simulation Experiments, *Proceedings of the IRE*, 48, 301–309, <https://doi.org/10.1109/JRPROC.1960.287598>,  
 1960.
- Ruti, P. M., Somot, S., Giorgi, F., Dubois, C., Flaounas, E., Obermann, A., Dell’Aquila, A., Pisacane, G., Harzallah, A., Lombardi, E.,  
 Ahrens, B., Akhtar, N., Alias, A., Arsouze, T., Aznar, R., Bastin, S., Bartholy, J., Béranger, K., Beuvier, J., Bouffies-Cloch  , S., Brauch, J.,  
 Cabos, W., Calmanti, S., Calvet, J.-C., Carillo, A., Conte, D., Coppola, E., Djurdjevic, V., Drobinski, P., Elizalde-Arellano, A., Gaertner,  
 920 M., Gal  n, P., Gallardo, C., Gualdi, S., Goncalves, M., Jorba, O., Jord  , G., L’Heveder, B., Lebeaupin-Brossier, C., Li, L., Liguori, G.,  
 Lionello, P., Maci  s, D., Nabat, P.,   nol, B., Raikovic, B., Ramage, K., Sevault, F., Sannino, G., Struglia, M. V., Sanna, A., Torma,  
 C., and Vervatis, V.: Med-CORDEX Initiative for Mediterranean Climate Studies, *Bulletin of the American Meteorological Society*, 97,  
 1187–1208, <https://doi.org/10.1175/BAMS-D-14-00176.1>, 2016.
- Sarghini, F., de Felice, G., and Santini, S.: Neural Networks Based Subgrid Scale Modeling in Large Eddy Simulations, *Computers & Fluids*,  
 925 32, 97–108, [https://doi.org/10.1016/S0045-7930\(01\)00098-6](https://doi.org/10.1016/S0045-7930(01)00098-6), 2003.
- Shahi, N. K., Polcher, J., Bastin, S., Pennel, R., and Fita, L.: Assessment of the Spatio-Temporal Variability of the Added Value on Precipi-  
 tation of Convection-Permitting Simulation over the Iberian Peninsula Using the RegIPSL Regional Earth System Model, *Clim Dyn*, 59,  
 471–498, <https://doi.org/10.1007/s00382-022-06138-y>, 2022.
- Skamarock, C., Klemp, B., Dudhia, J., Gill, O., Barker, D., Duda, G., Huang, X.-y., Wang, W., and Powers, G.: A Description of the Advanced  
 930 Research WRF Version 3, <https://doi.org/10.5065/D68S4MVH>, 2008.
- Stull, R. B., ed.: *An Introduction to Boundary Layer Meteorology*, Springer Netherlands, Dordrecht, ISBN 978-90-277-2769-5 978-94-009-  
 3027-8, <https://doi.org/10.1007/978-94-009-3027-8>, 1988.

- Sun, B., Feng, J., and Saenko, K.: Return of Frustratingly Easy Domain Adaptation, <https://doi.org/10.48550/arXiv.1511.05547>, comment: Fixed typos. Full paper to appear in AAAI-16. Extended Abstract of the full paper to appear in TASK-CV 2015 workshop, 2015.
- 935 Uguroglu, S. and Carbonell, J.: Feature Selection for Transfer Learning, in: *Machine Learning and Knowledge Discovery in Databases*, edited by Gunopulos, D., Hofmann, T., Malerba, D., and Vazirgiannis, M., vol. 6913, pp. 430–442, Springer Berlin Heidelberg, Berlin, Heidelberg, ISBN 978-3-642-23807-9 978-3-642-23808-6, [https://doi.org/10.1007/978-3-642-23808-6\\_28](https://doi.org/10.1007/978-3-642-23808-6_28), 2011.
- Vollant, A., Balarac, G., and Corre, C.: Subgrid-Scale Scalar Flux Modelling Based on Optimal Estimation Theory and Machine-Learning Procedures, *Journal of Turbulence*, 18, 854–878, <https://doi.org/10.1080/14685248.2017.1334907>, 2017.
- 940 Wolf, A., Saliendra, N., Akshalov, K., Johnson, D. A., and Laca, E.: Effects of Different Eddy Covariance Correction Schemes on Energy Balance Closure and Comparisons with the Modified Bowen Ratio System, *Agricultural and Forest Meteorology*, 148, 942–952, <https://doi.org/10.1016/j.agrformet.2008.01.005>, 2008.
- Zadra, A., Williams, K., Frassoni, A., Rixen, M., Adames, Á. F., Berner, J., Bouyssel, F., Casati, B., Christensen, H., Ek, M. B., Flato, G., Huang, Y., Judt, F., Lin, H., Maloney, E., Merryfield, W., Van Niekerk, A., Rackow, T., Saito, K., Wedi, N., and Yadav, P.: Systematic Errors  
 945 in Weather and Climate Models: Nature, Origins, and Ways Forward, *Bulletin of the American Meteorological Society*, 99, ES67–ES70, <https://doi.org/10.1175/BAMS-D-17-0287.1>, 2018.
- Zhang, G. P.: Neural Networks For Data Mining, in: *Soft Computing for Knowledge Discovery and Data Mining*, edited by Maimon, O. and Rokach, L., pp. 17–44, Springer US, Boston, MA, ISBN 978-0-387-69935-6, [https://doi.org/10.1007/978-0-387-69935-6\\_2](https://doi.org/10.1007/978-0-387-69935-6_2), 2008.
- Zhou, C. and Wang, K.: Evaluation of Surface Fluxes in ERA-Interim Using Flux Tower Data, *Journal of Climate*, 29, 1573–1582,  
 950 <https://doi.org/10.1175/JCLI-D-15-0523.1>, 2016.

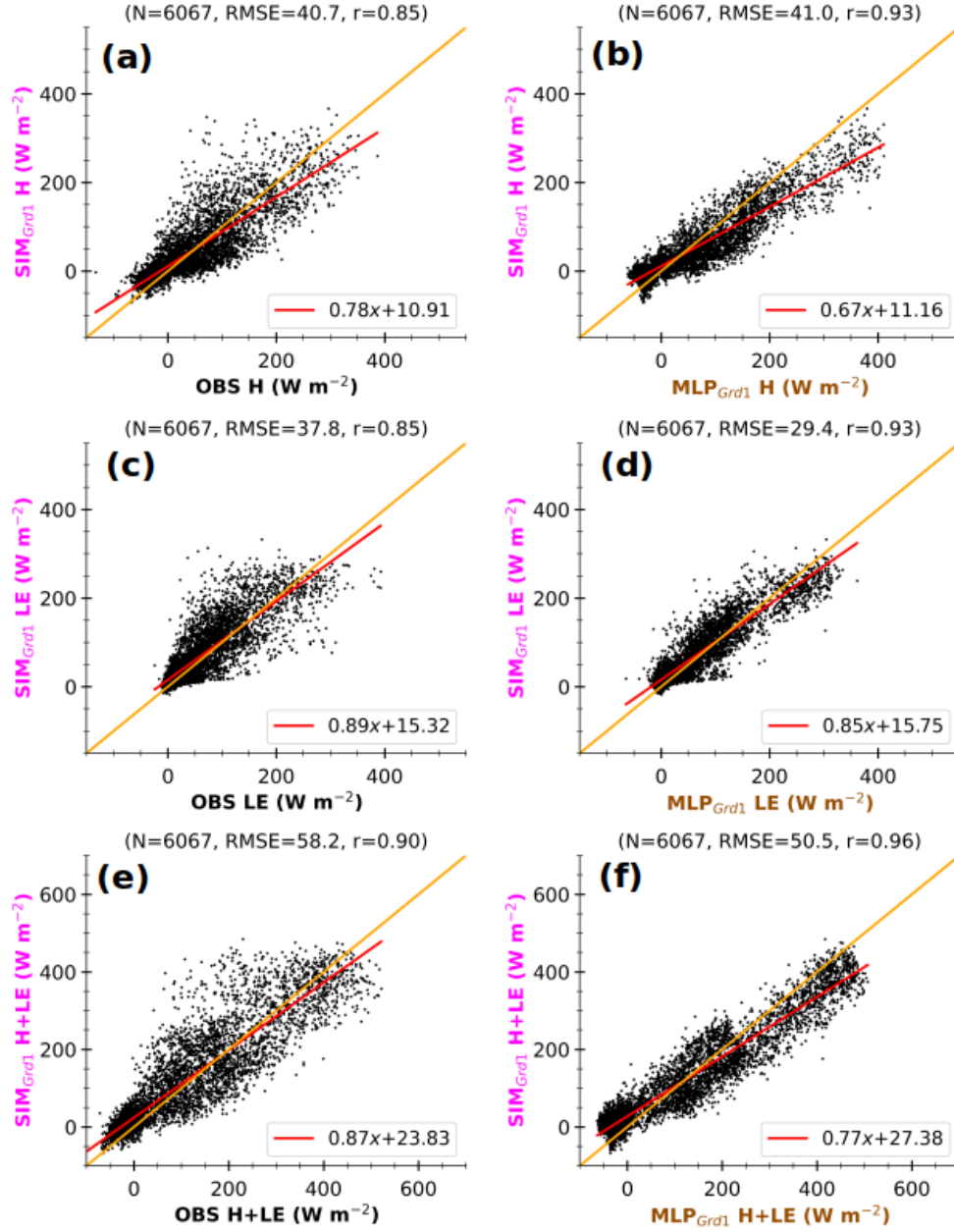


**Figure 12.** Comparison of 3-hourly-hour simulated fluxes at GrdPtGrd1, sensible heat flux ( $H$ , top panels  $SIM_{Grd1}$ ), latent heat flux with observed at the Météopole site ( $LE_{OBS}$ , middle-left panels) and total turbulent heat flux-MLP-based estimates in simulated environment ( $H+LE_{MLP_{Grd1}}$ , bottom-right panels) against observations for  $H$  (a and b),  $LE$  (c and d) and MLP-based fluxes under simulated environment  $H+LE$  (b, d-e and f). The data correspond to the same timestamps as in Figure 11 are also considered here. The values at the top of each panel correspond to the number of instances ( $N$ ), Root-Mean-Square-Error ( $RMSE$ ) and Pearson's correlation coefficient ( $r$ ). The lines in magenta-red and orange represent the linear and ideal fits, respectively. The axis labels are colored according to the schematic illustration in Figure 1.

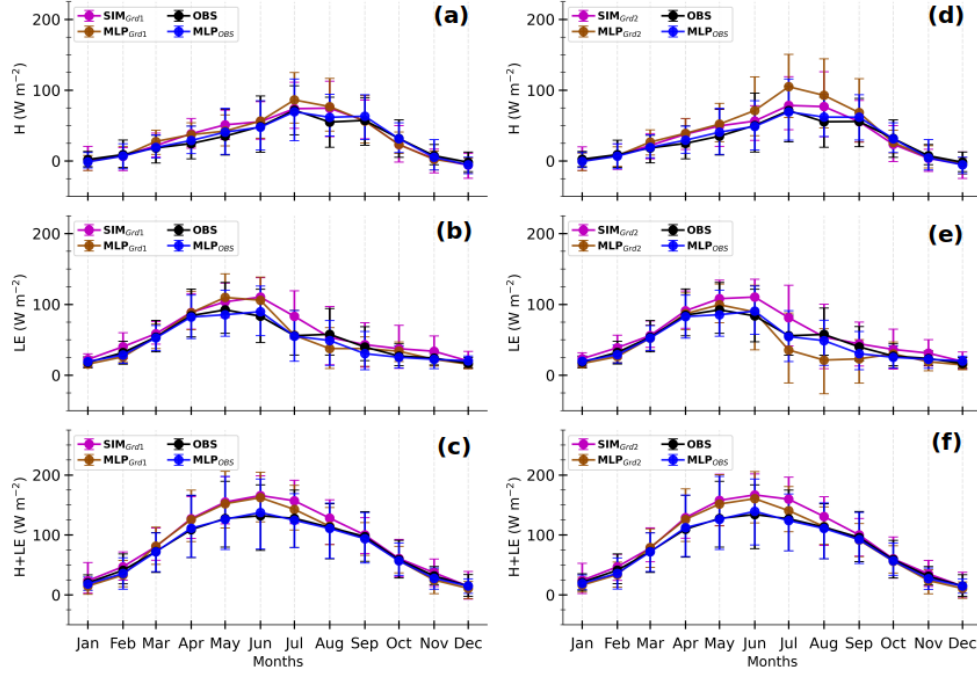


**Figure 13.** Composites-Composite monthly averages of simulated-sensible-heat flux ( $H$ , a and d), latent-heat flux ( $LE$ , b and e) and total-turbulent heat flux ( $H + LE$ , c and f) fluxes simulated at GrdPtGrd1 and GrdPtGrd2 (magenta-lines  $SIM_{Grd1}$  and  $SIM_{Grd2}$  in left and right panels respectively) and that of, MLP-based estimates for their respective observations environments ( $MLP_{Grd1}$  and  $MLP_{Grd2}$ ), observed at the Météopole site (black-lines  $OBS$ ) and MLP-based estimates in the observed environment ( $MLP_{OBS}$ ) for  $H$  (a and simulated environments-d),  $LE$  (cyan-b and orange-lines-respectively-e) and  $H + LE$  (c and f). The curve colours are according to the schematic illustration in Figure 1. The solid lines correspond to the means and the error bars represent the 10 and 90<sup>th</sup> percentiles, calculated by gathering the daily averages using 3-hourly-hour data. Only, the timestamps between 01 December 2012 and 31 December 2016 common to, for which both simulation and observational data are available, have been considered. The days involving less than 6 timestamps were excluded.